UNIVERSITY OF CALIFORNIA

Los Angeles

An Experimental Investigation of Two-Phase Crossflow Over Rigidly and Flexibly Mounted Tubes

A thesis submitted in partial satisfication of the requirements for the degree Master of Science in Mechanical Engineering

by

Susan Marie Gerhart

1991

The Thesis of Susan Marie Gerhart is Approved:

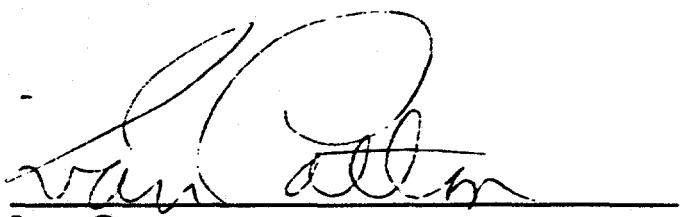

Ivan Catton

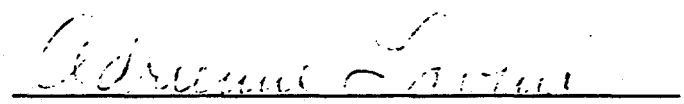

Adrienne Lavine

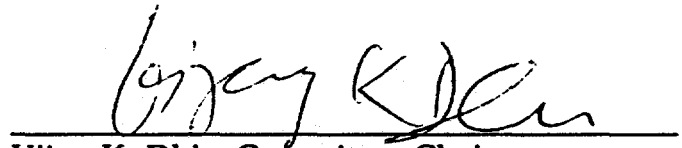

Vijay K. Dhir, Committee Chairman

University of California, Los Angeles

1991

TABLE OF CONTENTS

LIST OF FIGURES

LIST OF TABLES

LIST OF SYMBOLS

$A, A_{cross\text{-}section}$	Cross-sectional Area of the Test Section
C_D	Coefficient of Drag
C_L	Coefficient of Lift
D, d	Tube Diameter
f	Frequency
F_D	Drag Force
g	Gravitational Acceleration
m	Hydrodynamic Mass
P	Pressure
Q_A	Volumetric Flow Rate of Air
Q_l, Q_w	Volumetric Flow Rate of Liquid, Water
Re_l	Reynolds Number Based on Superficial Liquid Velocity
$Re_{l,gap}$	Reynolds Number Based on Superficial Liquid Gap (or Reference) Velocity
U	Velocity
U_{fs}	Liquid Freestream Velocity
U_l	Superficial Liquid Velocity
U_r, U_{ref}	Superficial Liquid Gap (or Reference) Velocity
W	Width of the Test Section

GREEK

α	Void fraction
α_{fs}	Free stream void fraction
δ	Partial derivative
Δ	Difference in pressure from that at lower stagnation point or small change

GREEK (Continued)

Δ^*	Difference in pressure from that at upper stagnation point
ν_L	Liquid kinematic viscosity
$\rho, \rho_g, \rho_L, \rho_w$	Density, density of gas, liquid, water
ϕ	Angle about tube, from lower stagnation point
ζ	Mass damping parameter

ABSTRACT OF THE THESIS

An Experimental Investigation of Two-Phase Crossflow

Over Rigidly and Flexibly Mounted Tubes

by

Susan Marie Gerhart

Master of Science in Mechanical Engineering

University of California, Los Angeles, 1991

Professor Vijay K. Dhir, Chair

Two-phase crossflow over heat exchanger tubes induces vibrations which contribute greatly to the wear on the tubes. Of the three mechanisms leading to two-phase flow-induced vibrations which have been identified, fluid-elastic instability has been recognized as that which leads to the vibrations with the largest amplitude. The mass damping parameter is used to predict the onset of fluid-elastic instability, and the mean drag coefficient is used to calculate the mass damping parameter. In this thesis, the drag coefficient measured over single tubes and tubes within array, in single-phase and two-phase flow at various Reynolds numbers, is discussed.

The drag coefficient was measured by two methods. For flexibly mounted tubes, strain gages were mounted on cantilever beams which held the tube in place and

allowed it to vibrate in the direction parallel to the flow only. For both rigidly and flexibly mounted tubes, pressure distributions were measured around the perimeter of the tube. Forces, and then the drag coefficient, could be calculated from this information.

The drag coefficient was not found to depend upon the flexibility of the tube mounting. As the void fracion of the flow increases, the drag coefficient over the tube increases. This effect was found to be quite large at low Reynolds numbers, and weaker at higher Reynolds numbers, and a different effect was found at very high Reynolds numbers.

I Introduction

Vibrations induced by two-phase crossflow over heat exchanger tubes have been recognized as a major cause of wear of the tubes found in steam generators, condensers, reboilers, and other heat exchangers found in nuclear power stations. The wear limits the current design lifetime of the tubes to about 30 years. The replacement of the tubes is quite costly, as it requires a shutdown of the facility. Thus, if the tube lifetime can be extended, the cost of nuclear power can be significantly reduced.

Three mechanisms leading to two-phase flow-induced vibrations have been identified. They are periodic wake or vortex shedding, random pressure fluctuations caused by turbulence at the wall, and fluid-elastic instability. Fluid-elastic instability results from a change in the angle of attack of the fluid, which in turn results from the tube vibrations. The amplitude of the self-excited vibrations due to fluid-elastic instability is much larger than for the other two mechanisms, and is caused by variations in the coefficients of drag and lift due to the altered flow field as the tube vibrates. The onset of fluid-elastic instability can be predicted using a correlation involving the mass damping parameter (Blevins,[1990]). Mean drag coefficient is used to calculate the mass damping parameter. Therefore, it is important to obtain measurements of the drag coefficient on tubes under two-phase crossflow.

The objective of this study is to develop a correlation for the dependence on certain parameters of the drag coefficient on a cylinder. These parameters include the

Reynolds number, the void fraction of the flow, and the ratio of the pitch between tubes to the tube diameter. Many parameters are involved in these vibrational mechanisms, and the mechanisms governing tube arrays cannot be properly understood without first developing a good understanding of those governing a single tube. Forces over a rigidly mounted tube are also of interest, because they can be compared to those over a flexibly mounted tube to distinguish the effects caused by our mounting techniques from those which are caused by the flow alone. This information is needed to compare the data to those of other researchers, as each utilizes different mounting techniques.

II Literature Search

Little work has been done on the drag coefficient of a blunt body subjected to two-phase flow. Yokosawa et al. [1986] measured the drag on a cylinder under two-phase crossflow, in the Reynolds number range of 4×10^3 to 3×10^5 and low void fractions (0 to 0.1). They measured the drag forces using pressure distributions on rigidly mounted tubes. Cantilever beam tube supports instrumented with strain gages were used for flexible tubes. These methods are similar to those used in this study which are described in section III of this document. Figure 1 is an example of their drag coefficient results for two-phase Reynolds numbers of 25000 to 130000, plotted versus void fraction. They define two-phase Reynolds number as:

$$Re_{TP} = \frac{U_{0.TP} D}{\nu_L} \tag{2.1}$$

where the freestream velocity $U_{0.TP}$ is defined as:

$$U_{0.TP} = \{2\Delta p_0 / [\rho_L(1-\alpha) + \rho_g(\alpha)]\} \tag{2.2}$$

and Δp_0 is the dynamic pressure of the main flow. Their results of the drag coefficients for both methods were equal, within reasonable error ($\pm$ 4%). They found that for two-phase Reynolds numbers sufficiently below the single-phase critical Reynolds number of 6.3×10^4, the drag coefficient decreased with increasing void fraction, while for Reynolds numbers above the critical value, the drag coefficient began to gradually increase with increasing void fraction, although it remained significantly less than the value for subcritical, single-phase flow. They correlated their

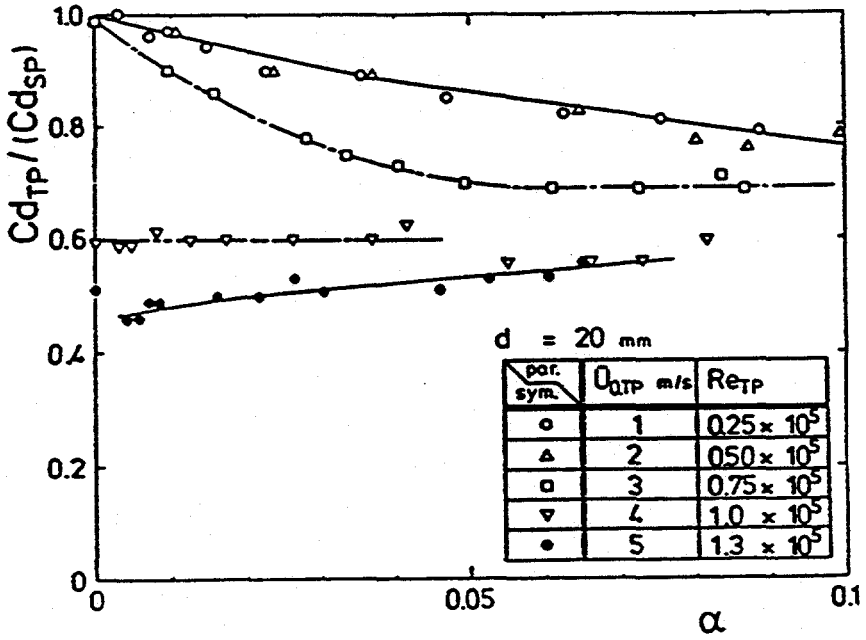

Figure 1. Coefficient of Drag vs. Void Fraction
Taken from Yokosawa, Kozawa, Inoue and Aoki (1986)

data to the following equations:

$$\frac{C_{DTP}}{C_{DSP}} = (0.60 + 0.40exp[-\alpha(8.67D/h)^6])[1 - 2.5\alpha(D/d_b)^{-1}] \qquad (2.3)$$

for $1.9 \times 10^4 \leq Re_{TP} \leq 6.3 \times 10^4$, and

$$\frac{C_{DTP}}{C_{DSP}} = 0.46 + 0.64\alpha^{3/4} \qquad (2.4)$$

for $1.3 \times 10^5 \leq Re_{TP} \leq 2.5 \times 10^5$, both for $0 \leq \alpha \leq 0.1$, where h is the width of the channel (D/h is the blockage), d_b is the mean bubble diameter, and $\frac{C_{DTP}}{C_{DSP}}$ is the ratio of the drag coefficient under two-phase flow conditions to that under single-phase flow conditions.

The first part of the same study (Inoue et al. [1986]) determined the void fraction distributions around the cylinder. They found a 4 or 5 fold increase in void fraction from the freestream value near the separation point, in a region which extended along the separation flow line into the wake, and a liquid-rich layer immediately upstream and downstream of the cylinder. They found that as the flow velocity was increased, the peak value of the void fraction increased at both the separation point and in the wake, and the peak position in the wake moved upstream. Also, the upstream liquid layer thickened while the downstream liquid layer thinned. When freestream void fraction was increased, they found that the only effect on the void profile was that the peak position for void fraction moved slightly downstream.

Hara has done a lot of research on two-phase crossflow over cylinders and arrays of cylinders, with the intent of minimizing flow-induced vibrations. In his work

concerning vortex-induced vibrations (1984), he found that by introducing a small amount of bubbles in crossflow, the cylinder vibrations could be decreased, while at larger void fractions, the bubbles excite the vibrations. Hara thought that the cause of this was that the random motion of the bubbles disturbed the cylinder's boundary layer and produced a random buffeting force.

Pettigrew et al. (1988), Taylor et al. (1986), and Taylor et al. (1988) discuss two-phase crossflow over tubes and tube bundles. In Taylor et al. (1986) they discussed forces over rows of tubes. They measured fluctuating forces on rows of tubes under crossflow with homogeneous void fractions, defined as $\alpha_H = \frac{Q_A}{Q_A+Q_W}$, varying from 0 to 0.95, and for pitch to diameter ratios of 1.5 and 3.0. The tubes they studied were 30 mm in diameter. They found that for single-phase flow, the fluctuations in lift dominate over those of drag, while the opposite was true for two-phase flow, and that the two-phase effect was magnified at the higher pitch to diameter ratio. Both the drag and lift coefficients were found to increase with increasing void fraction up to a void fraction of about 0.50, and then both coefficients decreased with increasing void fraction. Pettigrew et al. (1988) studied various tube array configurations, with pitch to diameter ratios of 1.47 and 1.32. Both a flexible tube in rigid bundle, and a bundle of flexible tubes were studied. They observed relatively stagnant zones of mostly liquid immediately upstream and downstream of each tube, with the two-phase mixture flowing around them, in a wake-like pattern.

They defined the fluidelastic instability factor K by the equation:

$$\frac{U_r}{fD} = K(\frac{2\pi\zeta m}{\rho D^2})^n \tag{2.5}$$

It was found that the instability factor decreased at the lower pitch to diameter ratio. Fluidelastic instability was found to occur at lower velocities with the arrays of all flexible tubes than for a flexible tube in the arrays of rigid tubes.

In Taylor et al. (1988), turbulence-induced vibrations for single tubes and single rows of tubes with various end conditions, were studied. The tubes had the same pitch to diameter ratios as in the previous part. They found that for low void fractions, the dynamic lift and drag coefficients were of the same magnitude, and the coefficients for single cylinders followed similar trends depending on void fraction and Reynolds number. Previous authors, including Taylor et al. (1986), Mulcahy (1984), and Savkar (1984), had found the lift coefficient to depend on Reynolds number an order of magnitude more strongly than the drag coefficient. Taylor et al. (1988) found the fluctuating forces to be strongest at a void fraction near 0.50 for arrays. For void fractions below 0.15, the lift and drag coefficients were found to be approximately the same as for single-phase flow.

Goyder (1988) has studied fluidelastic instability from a theoretical standpoint and supported his results with others' experiments. He concentrated on a square array of tubes, with fixed pitch and diameter. The tubes had flexible cantilever mountings and were allowed to vibrate in the lift direction. Void fraction varied from 0 to .93. He developed correlations for the excitation force, with and without

turbulence, based on both steady and fluctuating drag and lift coefficients, fluid properties, and tube dimensions. It was concluded that at low void fractions (up to .25), fluidelastic instability behavior is similar to that found for single phase flow, while at higher void fractions (.50 and higher), substantial vibrational amplitudes occur without threshold conditions to determine the onset of instability.

Work which involves forces on tubes under crossflow, but is limited to single phase flow, has been done by Fung (1960), Connors (1970), Price and Paidoussis (1984), Chen and Jendrzejczyk (1987), and Sin and So (1987). Fung measured steady and oscillating drag and lift forces on a large cylinder (12.65 inch diameter), subjected to an air crossflow, with Reynolds numbers of 3×10^5 to 1.4×10^6 using strain gage transducers. He found the oscillating lift force to be of the order of the mean drag force, and to be approximately constant at large Reynolds numbers. The mean lift force was found to be 0, and at large Reynolds numbers the mean drag coefficient was found to be around 0.25. Allowing the cylinder to oscillate had no effect on the oscillating lift force.

Connors also used strain gage transducers in his study of vibration of tube arrays. His tubes were tuned to different natural frequencies. and he studied normal square, rotated square, and parallel triangular arrays. He was mainly interested in the oscillating lift coefficient, as it is the main cause of the excitation mechanism. In the drag direction, he found a large steady component of the force, with a smaller fluctuating component superimposed. In the lift direction, he only found the alter-

nating component. When the vortex shedding frequency of the flow was below or at the tube's natural frequency, he found that the lift force oscillated predominantly at the shedding frequency. However, when the shedding frequency was sufficiently above the natural frequency, the lift force fluctuated at the natural frequency with the shedding frequency superimposed. The fluctuating drag force always oscillated at the tube's natural frequency.

Price and Paidoussis measured the drag and lift on one cylinder in a group of two or three cylinders under uniform crossflow. They varied the geometry and spacing between tubes in a range of Reynolds numbers of 1.7×10^4 to 8.6×10^4. They successfully predicted the tube response in this range by using superposition principals. For pairs of cylinders, they found the drag on the rear cylinder to be minimized when one tube was directly behind the other and the pitch to diameter ratio was 5.0. They found the drag on the front cylinder to be maximized when the rear tube was offset 0.2 diameters in the lift direction and 1.5 diameters in the drag direction. The lift force was found to increase as the rear tube was offset in the lift direction. The lift reached a maximum at 1.2 diameters for a drag directional offset of 5 diameters, but decreased thereafter. Experiments involving groups of three cylinders included the case of the test cylinder being positioned behind two cylinders which were both the same distance ahead of it in the drag direction. As the rear tube was moved in the lift direction, the drag was found to behave symmetrically, while the lift behaved antisymmetrically. The drag was minimized

when the rear tube was directly behind one of the front tubes.

Sin and So measured unsteady forces on a cylinder in an air crossflow by taking dynamic pressure distributions. They took data at a Reynolds number of about 4.8×10^4, and compared pressure differences along the span of the tube. Chen and Jendrzejczyk determined forces acting on a square array of tubes with a pitch to diameter ratio of 1.75 under turbulent crossflow. They measured the fluctuating drag and lift as a function of Reynolds number, incoming flow conditions, and the tube's location within the array. They found that the fluctuating lift and drag had similar frequencies, and that at low Reynolds numbers, the lift was periodic, while it was random at high Reynolds numbers. The lift was found to be greater than the drag, except for the front row tubes at Reynolds numbers below 3×10^4. They also found the forces on the first few rows to depend upon incoming flow conditions, while the system reached a steady state after 3 or 4 rows. Turbulence and forces were both found to increase with distance along the array.

III Experimental Apparatus and Procedure

In the present work, forces were measured over both flexibly and rigidly mounted cylinders of 2.2 cm outer diameter, and over a rigidly mounted cylinder of 1.9 cm outer diameter, under both single phase and two phase crossflow conditions. Water was used for the single phase flow, and a mixture of water and air was used for the two phase flow. Freestream void fractions tested have ranged from 0 to 42%. The 1.9 cm tube was measured as a single tube only, while the 2.2 cm tubes were tested both alone and within a parallel triangular array, as shown in Figure 2. The tubes in the array which were not being tested for drag were always rigidly mounted. These untested tubes were made 20 cm long and had plugs glued to each end. Each plug had a threaded hole in the center to fit a 1040 allan screw which held it in place through a small hole in the test section wall, as shown in Figure 3.

The tubes being tested extended through the walls of the test section, which is 20 cm inner diameter in the direction parallel to the cylinders, giving them an effective length of 20 cm. The rigidly mounted tubes were fixed to the walls of the test section, also shown in Figure 2. The 1.9 cm tube was bought as 3/4 inch stock acrylic tube, and the 2.2 cm tube was cut down, from 1 inch stock acrylic tube, using a lathe in the Student and Faculty Shop at UCLA. The tubes have an outer diameter tolerance of ± 0.015 inches. The depth of the inside of the test section is 12.5 cm in the direction normal to both the cylinders and the flow, and is 30 cm in height. Flow is in the vertically upwards direction.

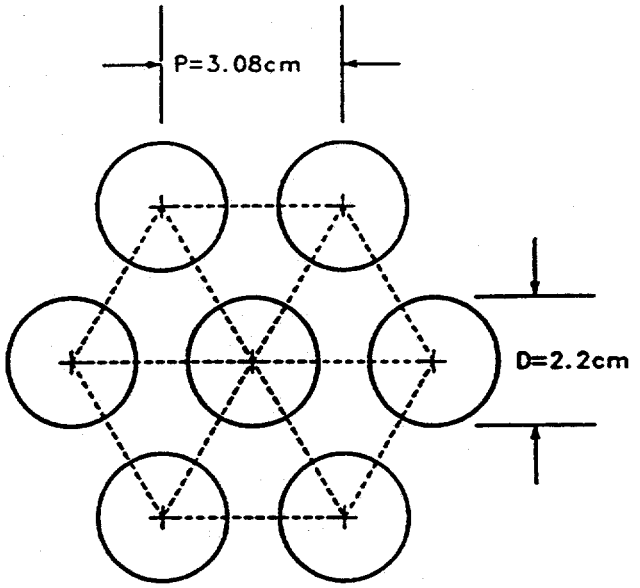

Grid Arrangement

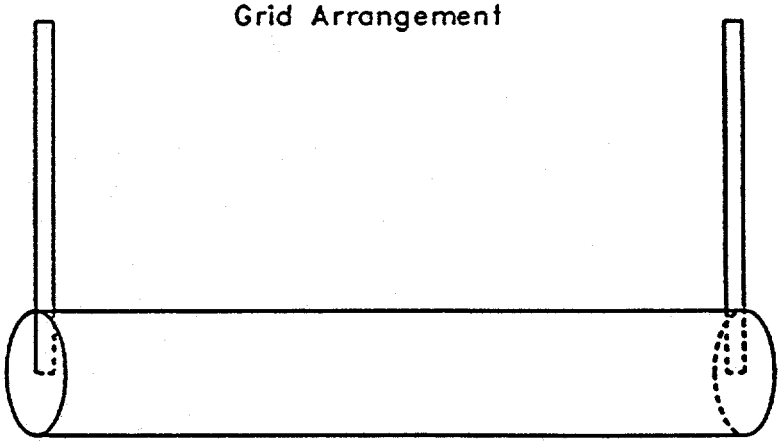

Central Tube – may be flexibly or rigidly mounted

Figure 2 – Parallel Triangular Array

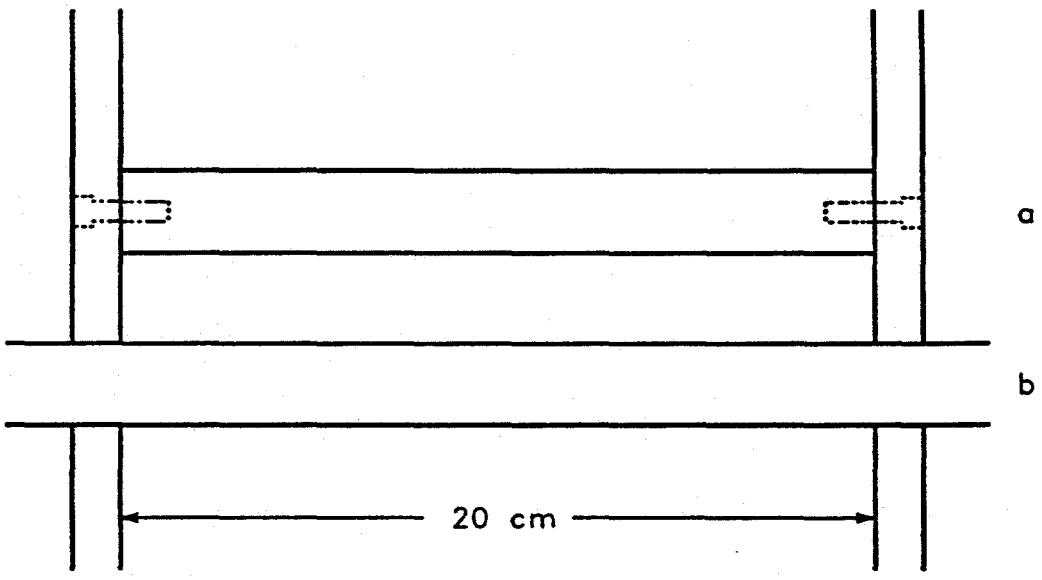

Figure 3 – Rigid Tube Mountings

a – array tube b – instrumented tube

A schematic of the flow loop is shown in Figure 4. It is primarily formed with 4 inch PVC pipe. The pump supplies water from the secondary reservoir to the pressure vessel. Utility air, which is available in the lab from the UCLA campus, is supplied above the water in the pressure vessel. A pressure regulator keeps it at a pressure of about 40 psi to maintain a constant flow rate from the vessel to the remaining sections of the loop. The flow exits the pressure vessel through a globe valve. Recently, a new pump has been installed. Most of the data have been taken with a 300 GPM pump, but data at the highest Reynolds numbers have been taken with the newer, 1000 GPM capacity pump. After passing through the globe valve, the pipeline for the older pump leads to a turbine flow meter, and the pipeline for the newer pump is split to lead to two turbine flow meters running in parallel. The additional line for the newer pump is indicated by dashed lines in Figure 4, and the parallel lines are rejoined before the next section of pipe. Water flow is then turned upwards to flow vertically through the test section segment of the flow shown in Figure 5. If two phase flow is desired, utility air is introduced through one or more injection holes. For each injection hole, air enters a flow meter through a gate valve. It passes a pressure gage, which is used to correct the measured flow rate, and a ball valve releases it to the water. The bubbles are broken up to an average size of 3.6 mm diameter by a series of wire meshes which homogenize the mixture before it enters the diffuser. After expansion in the diffuser, which expands at angles of 7 degrees, the flow is straightened in the flow development section. The flow development section is 30 cm high, and has the same dimensions as the test section.

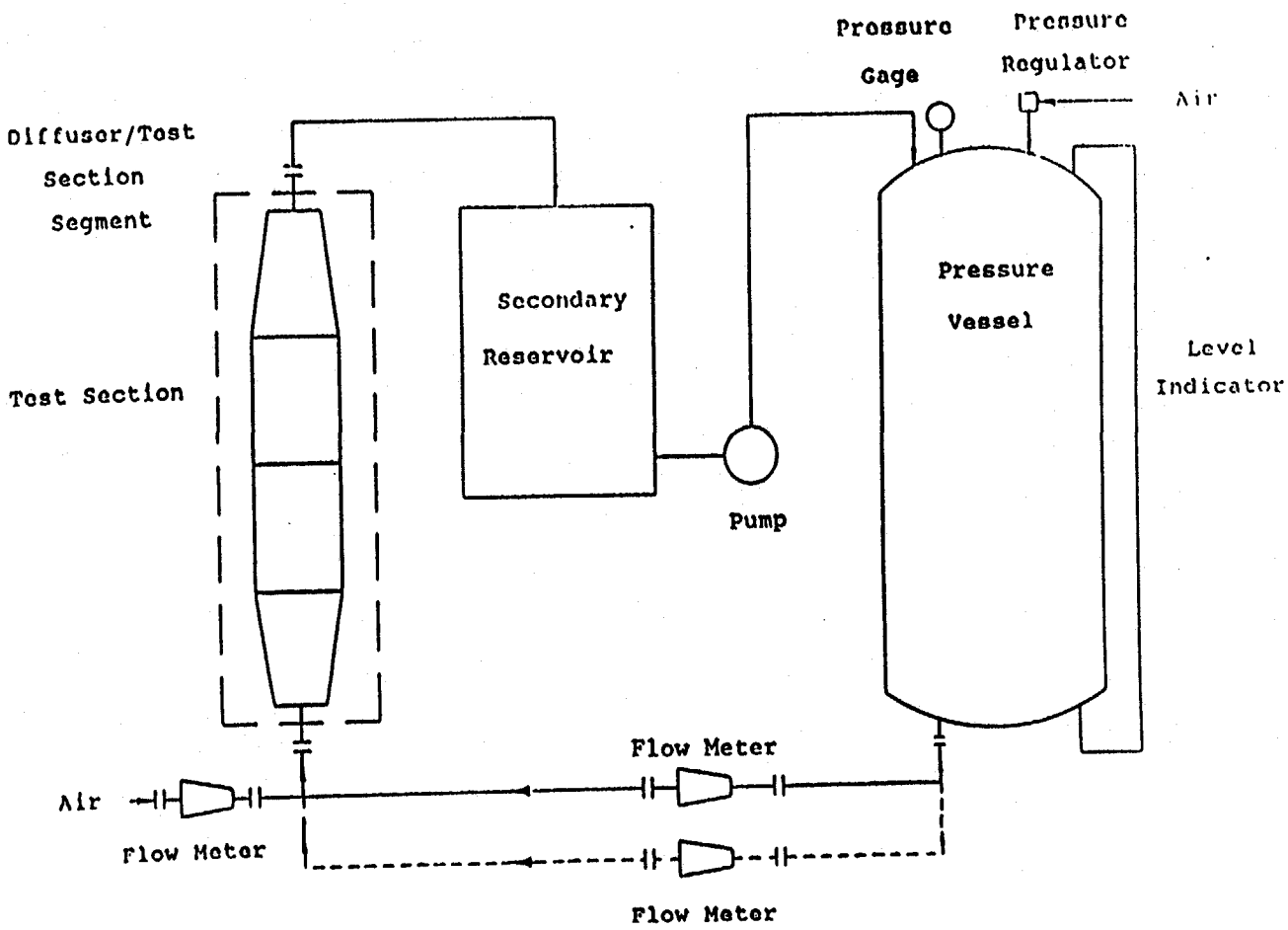

Figure 4. Schematic Diagram of The Loop

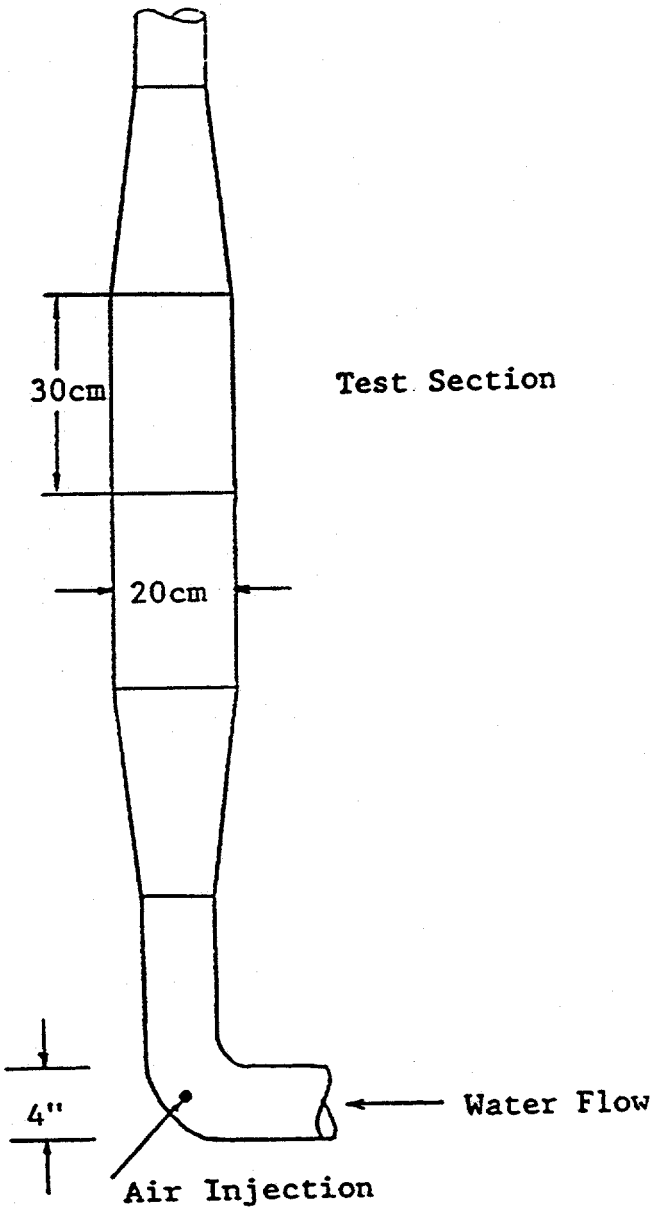

Figure 5. Test Section Segment

The flow exits through a converging section which is identical to the diffuser, and is then released to the secondary reservoir, where air is allowed to escape.

The test section segment of the flow is constructed of half inch plexiglass sheet. This allowed the use of photography to visualize the flow, and a gamma densitometer to measure the time-averaged void fraction at various positions, providing information on the existence of a wake downstream of the cylinder and the freestream void fraction. The gamma densitometer consists of a cesium-137 source and an NaI detector. The gamma beam created by the source is collimated by passing through a small opening in the source's lead housing. It then passes through the test section, and it is again collimated by passing through a small opening in the detector's lead housing. More rays pass through air than through water. Gamma rays are absorbed in the detector, producing electronic pulses which are passed on to a single-channel analyzer. A 1024-channel analyzer sorts the pulses into different channels, depending on the energy of each pulse, and stores them. The number of pulses is plotted versus channel number, and the integral under the curve (I) is calculated within the region of interest among the channels. The value of I is recorded and used to calculate the void fraction using the following equation:

$$\alpha = \frac{ln(I/I_l)}{ln(I_a/I_l)} \tag{3.1}$$

where I_l is the integral under the curve in the case of pure liquid, and I_a is in the case of pure air, and all integrals are for the same time period. The gamma densitometer must be calibrated before each run, because each time it is moved

with respect to the test section, the gamma beam goes through the test section at a different angle with respect to the walls (see Figure 6), and a different amount of the beam is attenuated with the contents of the test section. In general, the calibration time period is longer than the two-phase flow run time. The integrals may be normalized by dividing by the run time. For instance, usually the calibration is run for 100 seconds each for pure water and pure air, but the actual experiment is run for only 30 seconds for two-phase flow. In the equation, the time difference in the denominator cancels, but not in the numerator. The value of I_l used in the numerator is normalized by multiplying it by 30/100 before it is inserted into the equation, so the actual equation used is:

$$\alpha = \frac{ln(I/.3I_l)}{ln(I_a/I_l)} \tag{3.2}$$

The rigidly mounted tube is instrumented with pressure taps to measure the drag coefficient. The distribution of the pressure taps about the tube is shown in Figure 7. The 1.9 cm tube has two pressure taps, which are located 180° from each other, and are .125 inches in diameter. In each tap, a teflon tube of 1 mm inner diameter and .079 inches outer diameter is inserted, with a 0.4 inch long collar of tygon tubing .063 inches inner diameter and .125 inches outer diameter holding it tight in the tap. The tubing and the collar are inserted from the outside of the cylinder to the inside of it, and then any tubing extending beyond the cylinder diameter is cut flush to it, resulting in the configuration shown in Figure 7. The teflon tubing extends through the center of the cylinder and out of the test section,

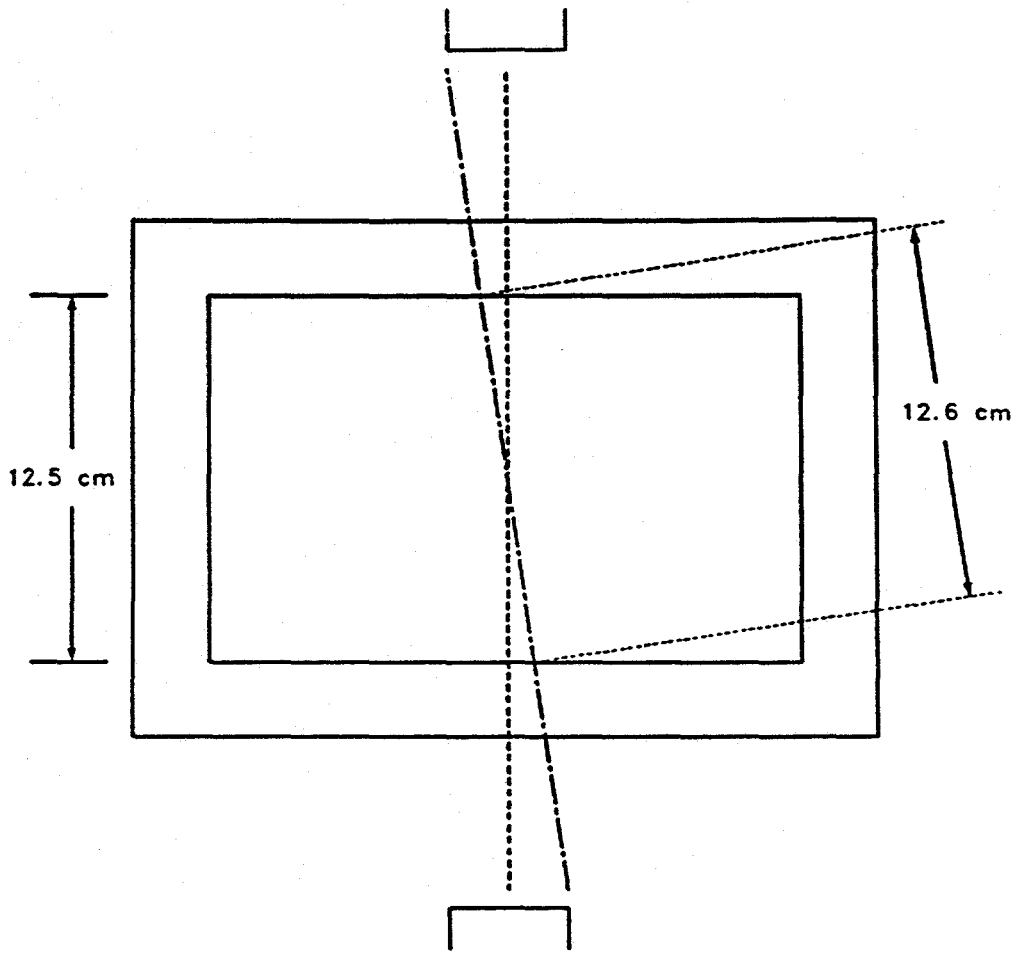

Figure 6 – Gamma Beam Positions

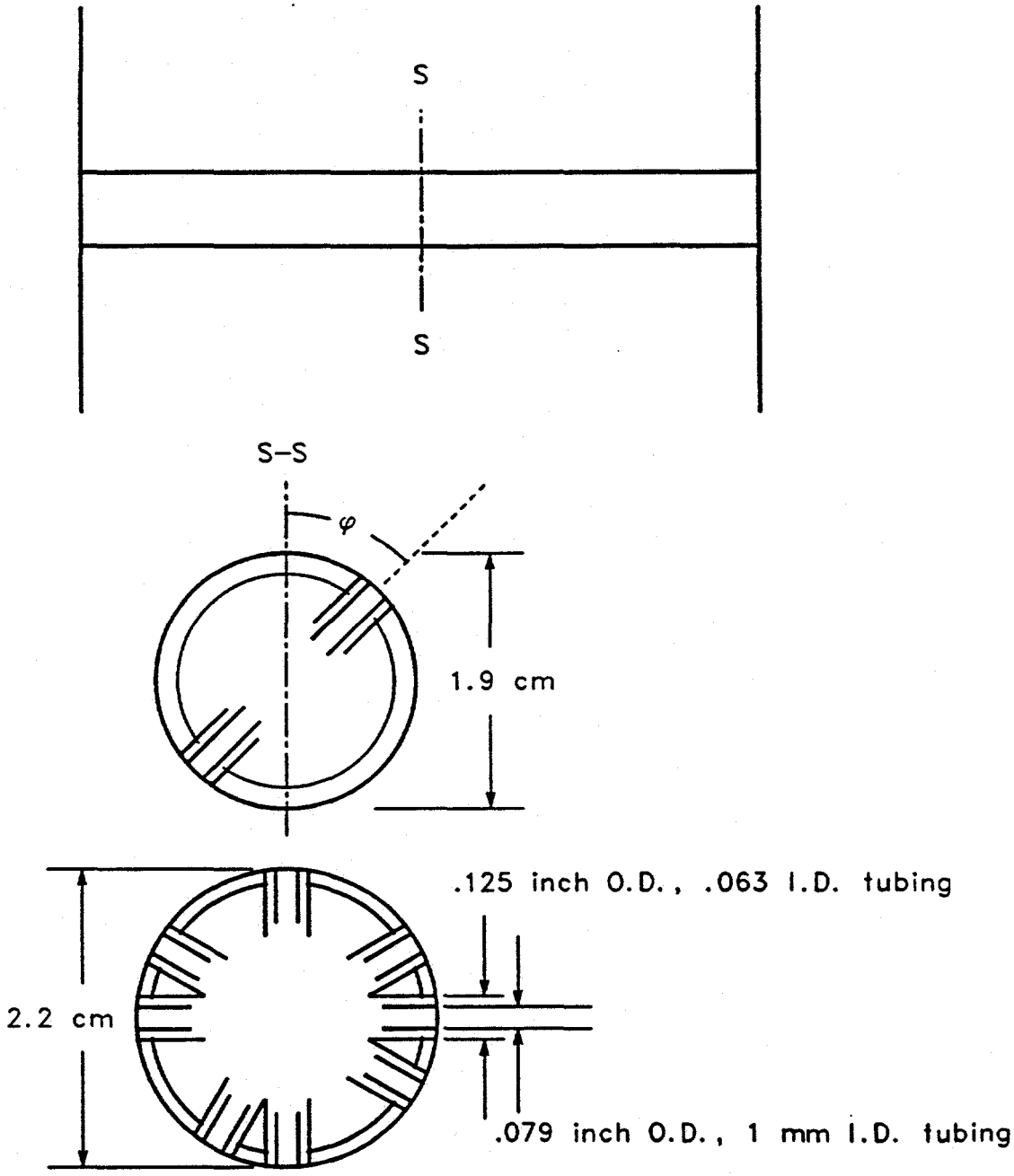

Figure 7 – Pressure Tap Distribution

where it is expanded through a reducing union to a .125 inch inner diameter and .250 inch outer diameter polyethelene tubing. Through the polyethelene tubing, the taps lead to an inclined .13 inch inner diameter glass manometer which gives the pressure difference between the two. After a few experiments, it was determined that it was impossible to keep bubbles of air from slipping into the taps along with the water which filled the tubing as the liquid level changed due to change in pressure difference. Because air is compressible, any bubbles must be removed from the line if we are to read an accurate magnitude of the pressure. To accomplish this, we installed a valve at each line of polyethelene tubing which allows the tap to be connected either to the manometer or to a pressurized water source which would push the bubbles back out. The pressure difference of the taps under static conditions is measured with the taps located horizontal from each other. Once the flow conditions have been set, the tube is turned to provide angles between the taps and the direction of the flow of 0°, 22.5°, 45°, 67.5°, and 90°, and the pressure difference between the two is measured at each angle. The static pressure is subtracted from the pressure under crossflow to give the value of the pressure difference caused by the flow alone. This value is multiplied by the cosine of the angle between the taps and the flow, and then integrated over the angle, ϕ. The drag coefficient is calculated using the following equation:

$$C_D = \frac{2gD}{U_l^2}\left(\frac{\pi\alpha}{4} + \int_0^{\pi/2} C_1 \frac{\Delta}{D} cos\phi d\phi\right) \tag{3.3}$$

where C_1 depends upon the angle that the manometers are inclined from the horizontal. (See Appendix 3 for the derivation.)

The 2.2 cm tube has pressure taps located at angles of 0°, 30°, −60°, ±90°, ±120°, and 180° from the lower stagnation point. Each tap is .125 inches diameter. A .063 inch inner diameter and .125 inch outer diameter tygon tubing is inserted inside each tap in a manner similar to the method used with the 1.9 cm tube. Another 1 mm inner diameter, .079 inch outer diameter teflon tubing is inserted to minimize the number of bubbles entering the tube during the run. Outside the test section, the tubing is again expanded through a reducing union to .125 inch inner diameter and .250 inch outer diameter polyethelene tubing. A tap at the lower stagnation point is connected to each of the remaining taps through a manometer, and as with the 1.9 cm cylinder, each line has a valve for the expulsion of any bubbles in the line. The drag coefficient is calculated using the equation:

$$C_D = \frac{gD}{U_l^2}\left(\frac{\pi\alpha}{2} + \int_0^{2\pi} C_1 \frac{\Delta^*}{D} cos\phi d\phi\right) \tag{3.4}$$

and the lift coefficient is calculated using the equation:

$$C_L = -\frac{gD}{U_l^2}\int_0^{2\pi} C_1 \frac{\Delta^*}{D} sin\phi d\phi \tag{3.5}$$

Reynolds numbers (Re_l) have been tested in the range of 371 to 21854 for a single tube, and in the range of 5883 to 32683 for a tube in an array, based on

superficial liquid velocity in the test section and the superficial liquid gap velocity, respectively. The flow meters are calibrated to give volumetric flow rate, and velocities are calculated by dividing the flow rate by the cross- sectional area of the test section. For a triangular array, the liquid gap velocity is usually calculated using the equation

$$U_{ref} = \frac{P}{P-D} U_{fs} \tag{3.6}$$

The correction is based on the reduction of the cross-sectional area of the flow in an infinite array by the insertion of the tubes. (See Figure 8a.) However, the array used in these experiments does not include enough tubes to be considered infinite. As such the decrease in cross-sectional area, and hence the increase in velocity at the gap, are not as large. As can be seen from Figure 8b, the actual gap velocity may be calculated using the equation

$$U_{ref} = \frac{W}{W-nD} U_{fs} \tag{3.7}$$

where n is the number of tubes in the row. For our array, the test section is 12.5 cm wide, and the tube being tested is in a row of three 2.2 cm diameter tubes, so $U_{ref} = 2.12 U_{fs}$.

The same test section is used for flexibly mounted tubes as for rigidly mounted tubes. The 2.2 cm flexibly mounted tubes were attached to cantilever beams

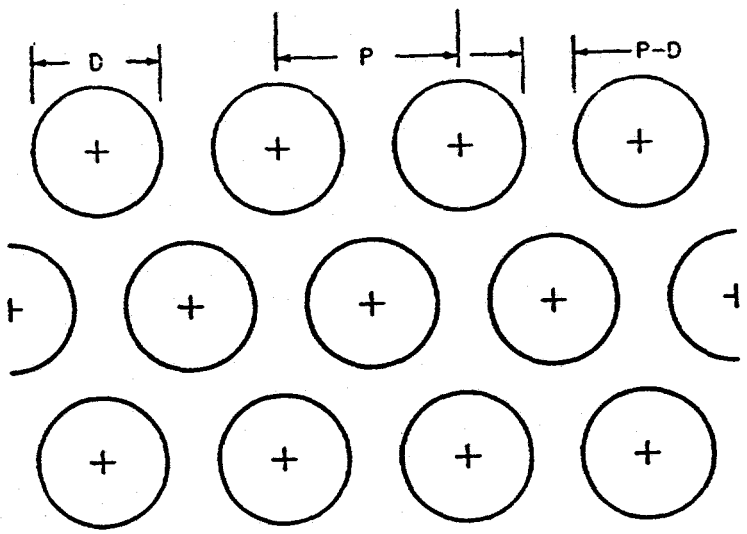

Figure 8a – Reduced Area of Infinite Array

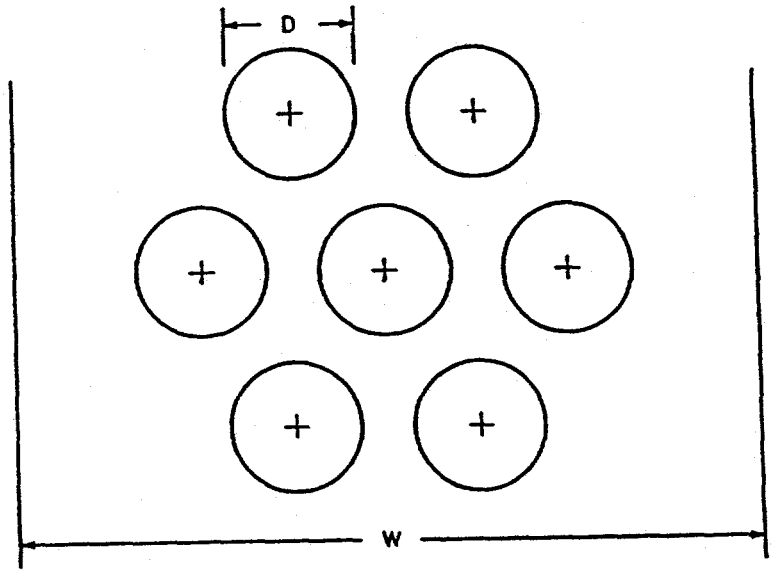

Figure 8b – Reduced Area of Limited Array

mounted just outside the test section, and had cups over them to keep the water in. This setup is shown in Figure 9. This method was used, rather than simply putting the cantilever beams inside the test section, to prevent the cantilevers from interfering with the flow, as well as to keep the flow from directly affecting the cantilever beams, which were sometimes instrumented with strain gages as described below.

The vibrations of the flexibly mounted tube are quite large. For this reason, only the freestream void fraction could be obtained. The accuracy in location desired for a local void fraction is within a smaller distance than the vibrational amplitude, and the run time during which the gamma densitometer signal is integrated is much longer than the period of vibration of the tube, so a void fraction profile of a flexibly mounted tube would not be as meaningful as a profile of a rigidly mounted tube.

The drag coefficient on a flexibly mounted tube is measured in two ways. The pressure distribution is taken in exactly the same way as for a 2.2 cm rigidly mounted tube, and strain gages are installed on the cantilever beams supporting the tube. The strain gages used are CEA-06-125UN-120 strain gages. The cantilever beams are constructed of .018 inch thick spring steel and are 6 mm wide. The strain gages are located 5.0 cm from the center of the tube, giving the beams an effective length of 5.0 cm from the applied force to the gage. Two gages are installed on each cantilever, one on the tension side, one on the compression side. The strain gage signal is sent to a 3800 wide range strain indicator, and the wheatstone bridge is

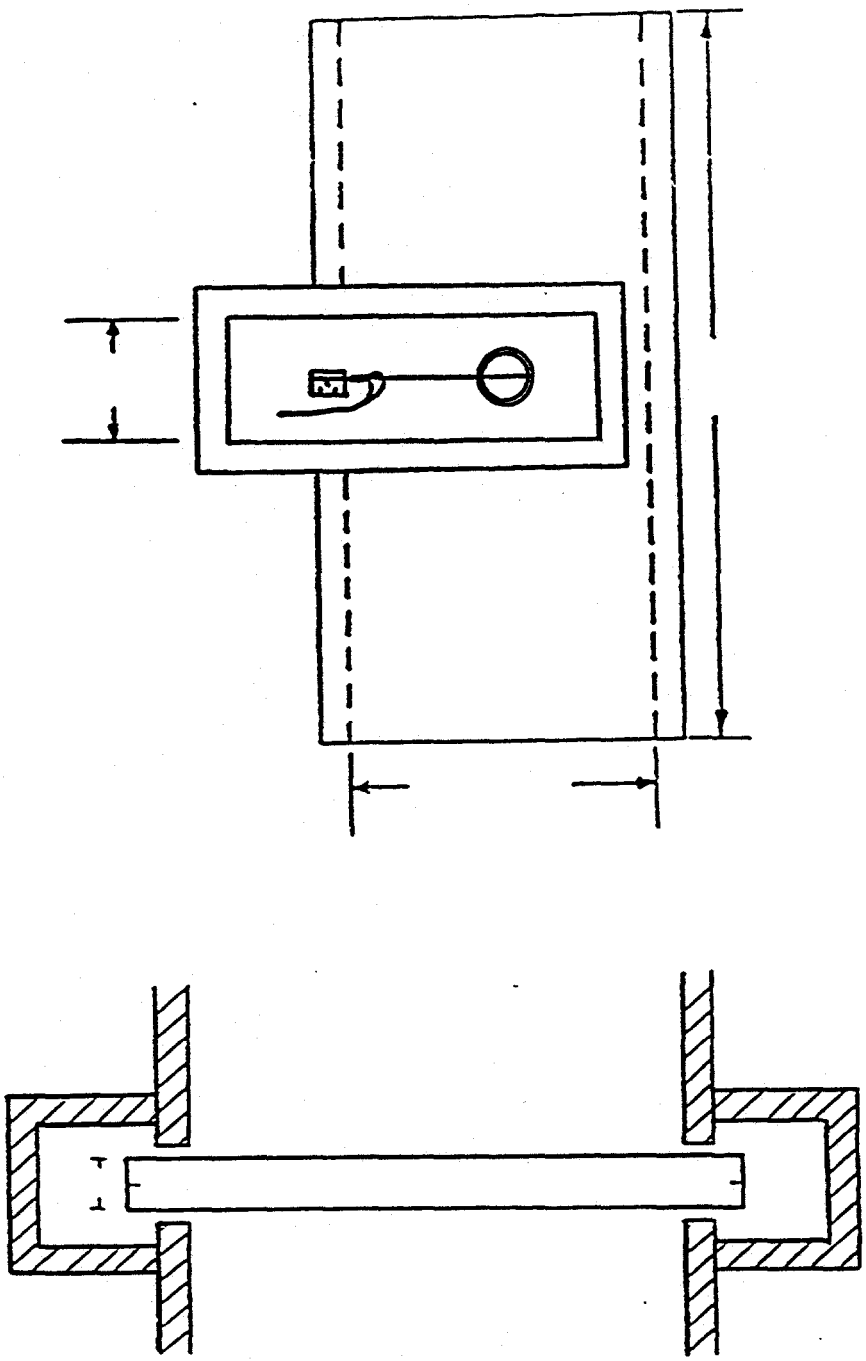

Figure 9. Flexible Tube Mounting

zeroed with the test section sideways to minimize the strain on the gages at the calibrated zero. The gages are also calibrated in this configuration, to keep the calibration curve within the range at which the strain gage response is linear. The calibration is performed by putting static loads on the tube, in both the upstream and the downstream directions, and noting the resulting strain. An example of a typical calibration curve is given in Figure 10.

The strain indicator is connected to a chart recorder, which records strain as a function of time. From this, the mean value of the drag over the tube can be obtained, as well as the amplitude of vibration. The strain indicator can also be connected to a spectrum analyzer to get data on the frequencies of vibration of the tube. When the strain gages are used to calculate the drag coefficient, the test section is first filled with water. The flow is stopped, and while the tube is at rest the chart recorder is run to plot the constant strain on the system as the zero value. The water flow is then started at the desired liquid velocity, and the air is added, if two-phase flow conditions are desired. Then, the chart recorder is run again, on the same chart, to plot the varying strain on the system under flow conditions. To obtain the drag, several regions of the strain-time plot are chosen for analysis. In each region, each peak and valley of the curve is measured to determine its distance from the zero value. The mean height is calculated within each region, and the corresponding strain and force are calculated. The height, strain, and force are averaged over all of the regions chosen for the given conditions. A comparison of the values obtained for

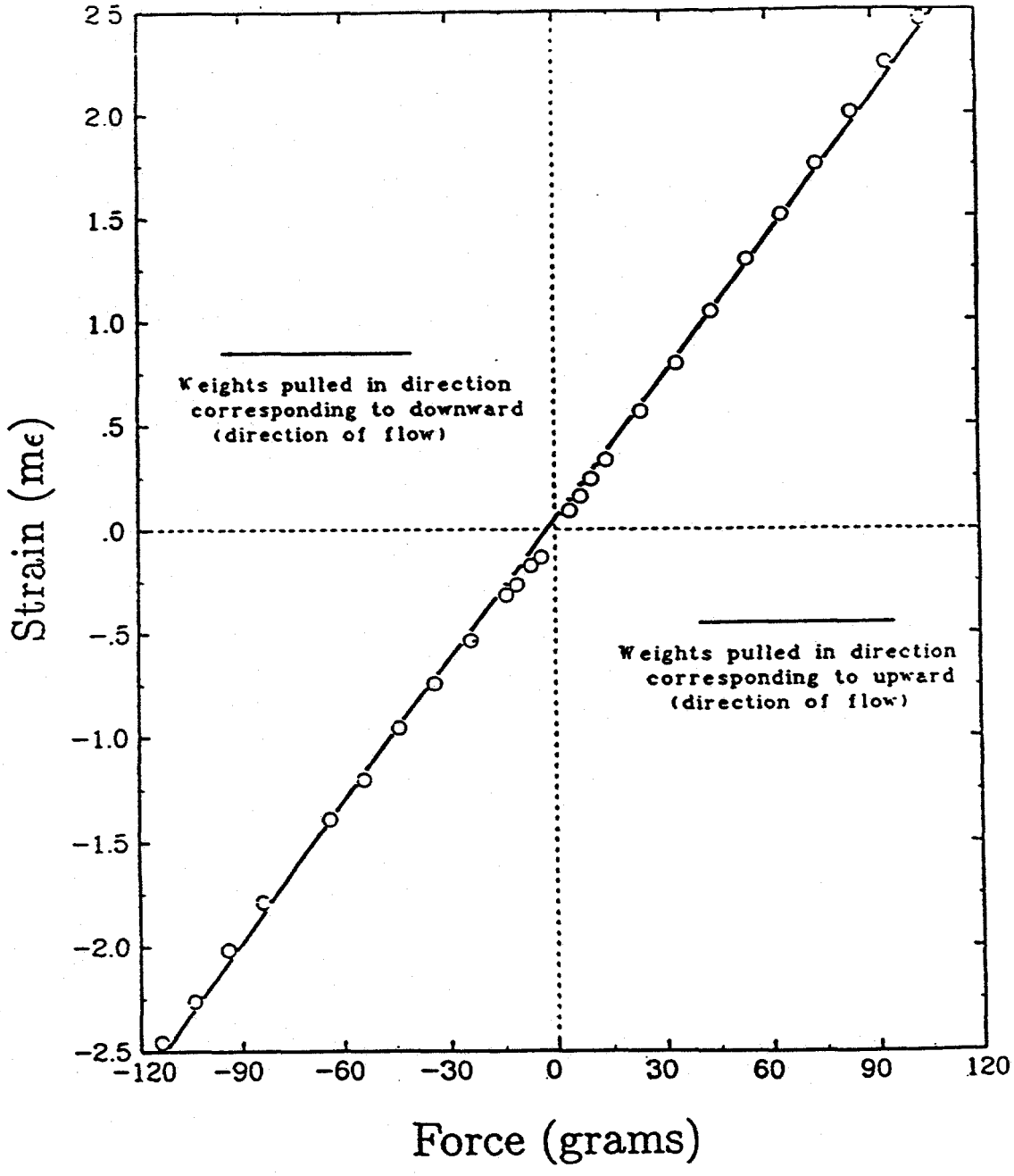

Figure 10. Strain Gage Calibration Curve

the individual regions gives the uncertainty of our measurements. The difference in the buoyancy force acting on the tube submerged in pure liquid, and the buoyancy force on the tube in the two-phase mixture is added to the force calculated from the plots, and the result is the net drag force.

The flexibly mounted tube weighs 0.0775 kg. Reynolds numbers in the range of 428 to 8226 have been tested for a single flexibly mounted tube, and in the range of 4703 to 17428 for a flexibly mounted tube in an array.

IV Discussion of Results for a Rigidly Mounted Tube

For a rigidly mounted tube, observations were made of drag coefficient, lift coefficient, pressure distribution, and void fraction profile. The data are tabulated in Tables 2A to 2D of Appendix 2.

The coefficients of drag on a single rigidly mounted tube are plotted versus void fraction, on a semilog scale, for various Reynolds numbers, in Figure 11. Increasing void fraction is found to very strongly increase the drag coefficient at lower Reynolds numbers, and to more weakly increase the drag coefficient at higher Reynolds numbers. At a Reynolds number of 428, the drag coefficient for a void fraction of 17% is about 450. This is about 375 times 1.2, the value for single-phase water flow. At the same Reynolds number, the drag coefficient for a void fraction of 36% is 717, about 600 times the value for single-phase flow. For a Reynolds number of 8226, and a void fraction of 36%, the drag coefficient is 4.3, which is only about 4 times 1.1, which is the value for pure water flow. This is a much smaller increase than that at the smaller Reynolds number, although it is quite a substantial one. For a Reynolds number of 21854, however, the drag coefficient at a void fraction of 4.6% is only 0.81, which is actually less than (about 0.6 times) the single-phase value of about 1.3. This shows that the effect of void fraction on the drag coefficient undergoes a change at very high Reynolds numbers. As the void fraction is further increased, the drag coefficient does begin to increase again, though, up to 1.99 for a void fraction of 24%, which is a drag coefficient of about 1.6 times the single-phase

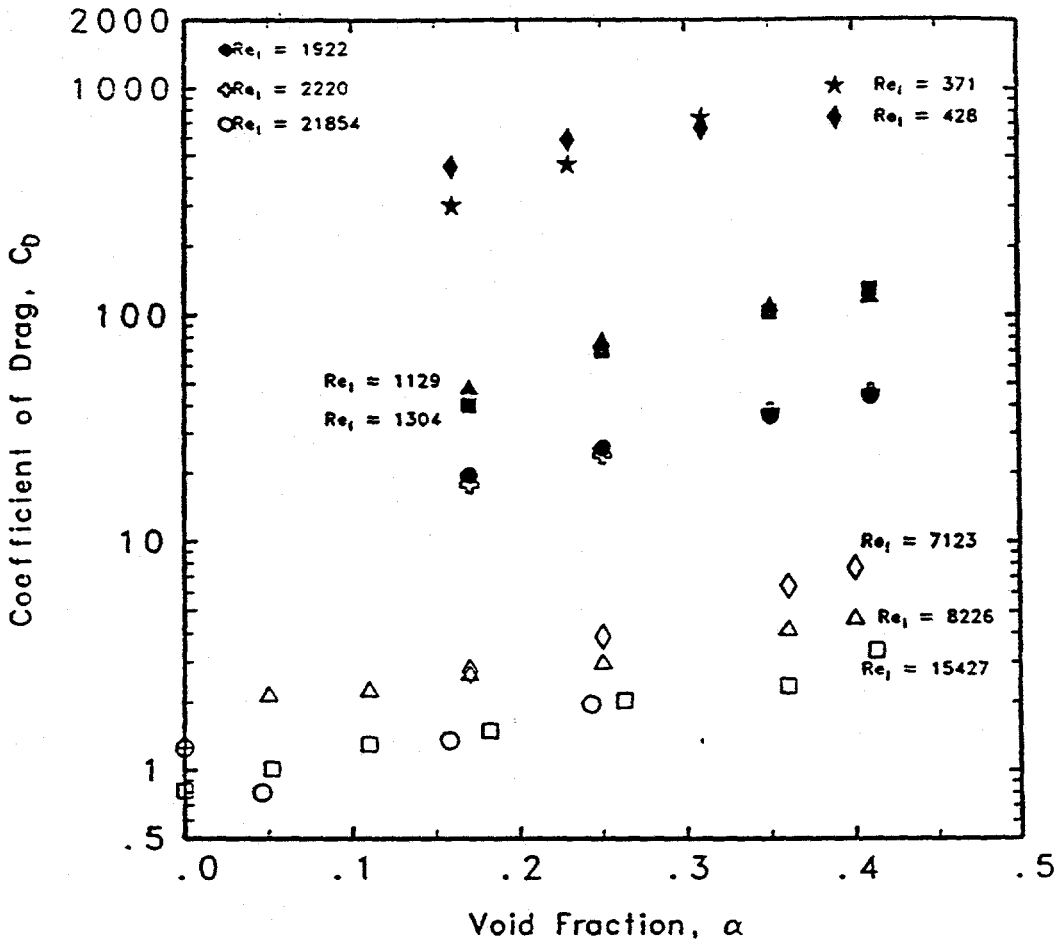

Figure 11 – Coefficient of Drag Over a Single Rigid Tube

value.

In Figure 12, the drag coefficient data are again plotted, this time versus Reynolds number for various void fractions, including 0.0, and on a log-log scale. The lines plotted through the data are the curves fitted using the least squared method. Plotted on the same figure is the well established correlation found by Roshko, (see Sabersky, Acosta, and Hauptmann [1971]). The drag coefficients obtained at zero void fraction were within 15% of the correlated values.

The pressure distribution for a Reynolds number of 8226 and a void fraction of 0.25, found by the pressure taps, is plotted in Figure 13, going around the tube starting at the lower stagnation point. The pressure plotted is the difference in pressure from that at the upper stagnation point. The drag coefficient was obtained by taking the integral of the pressure multiplied by the cosine of the angle around the tube. Although the lift coefficient is always expected to be zero by theory, it could similarly be obtained by taking the integral of the pressure multiplied by the sine of the angle around the tube. The slight asymmetry of Figure 13, which was also found in the void profiles, is the cause of the non-zero lift measurement. The magnitude of the lift coefficient is indicative of the extent of error in the drag data, and is included in Appendices 1 and 2. The lift is at least an order of magnitude less than the drag at high velocities, and is at least two orders of magnitude less than the drag at lower velocities.

In Figure 14, data taken by Yokosawa et al. (1986) have been plotted in a similar

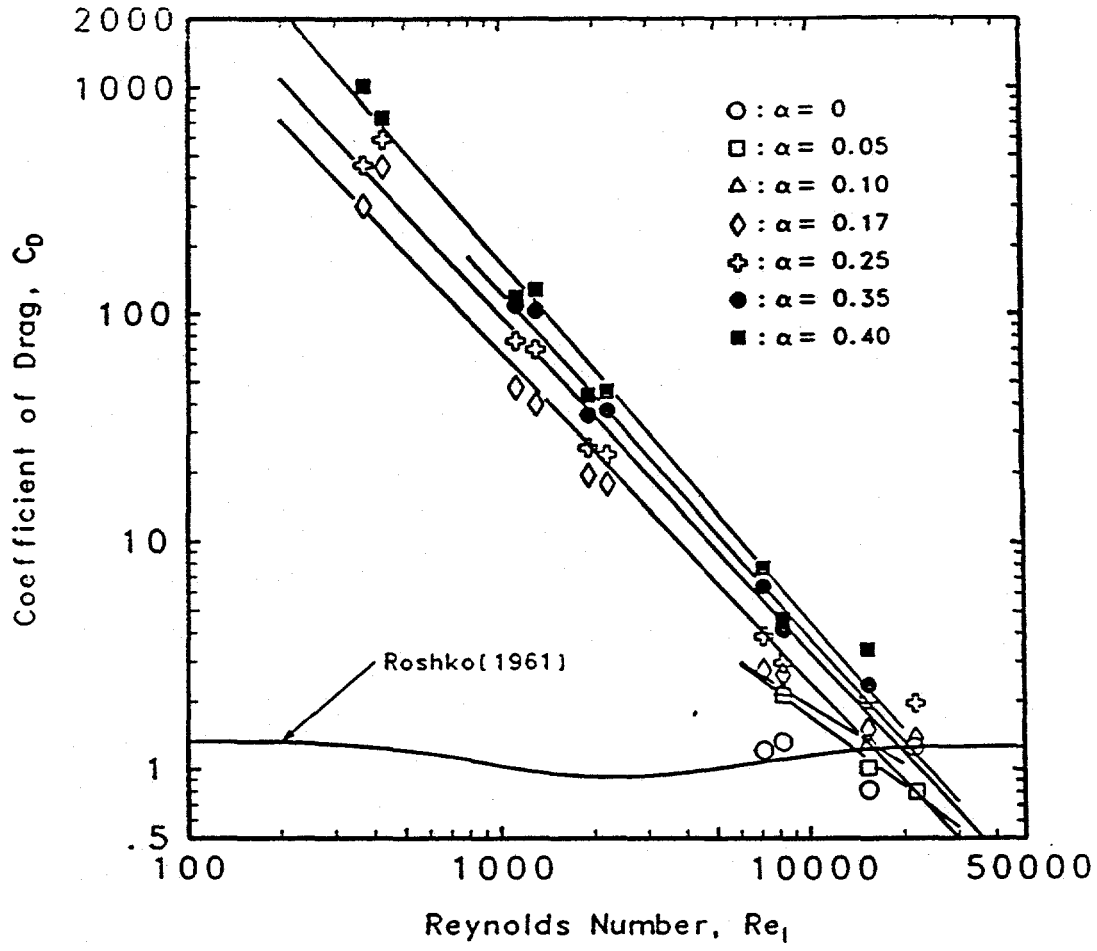

Figure 12 – Coefficient of Drag Over a Single Rigid Tube

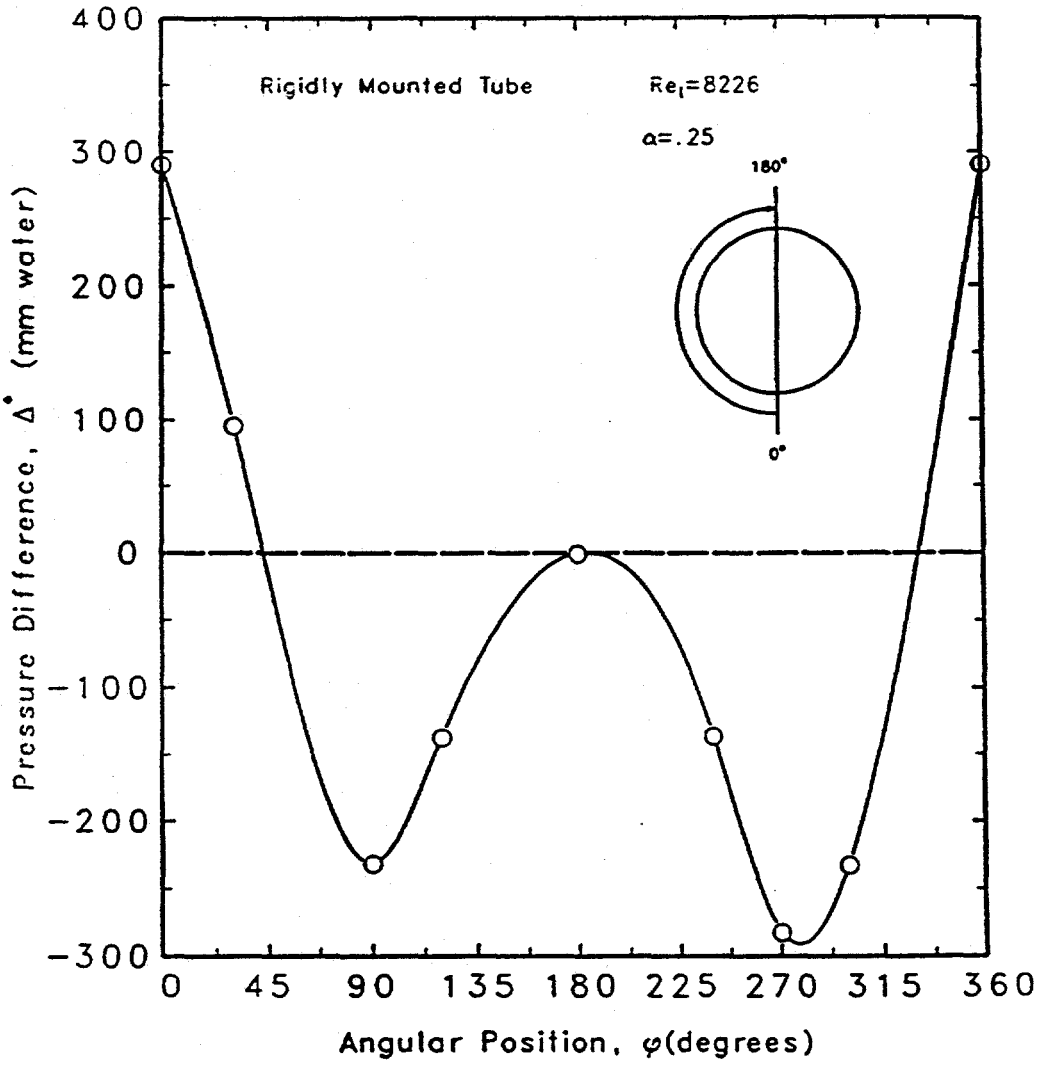

Figure 13 – Pressure Distribution About Tube

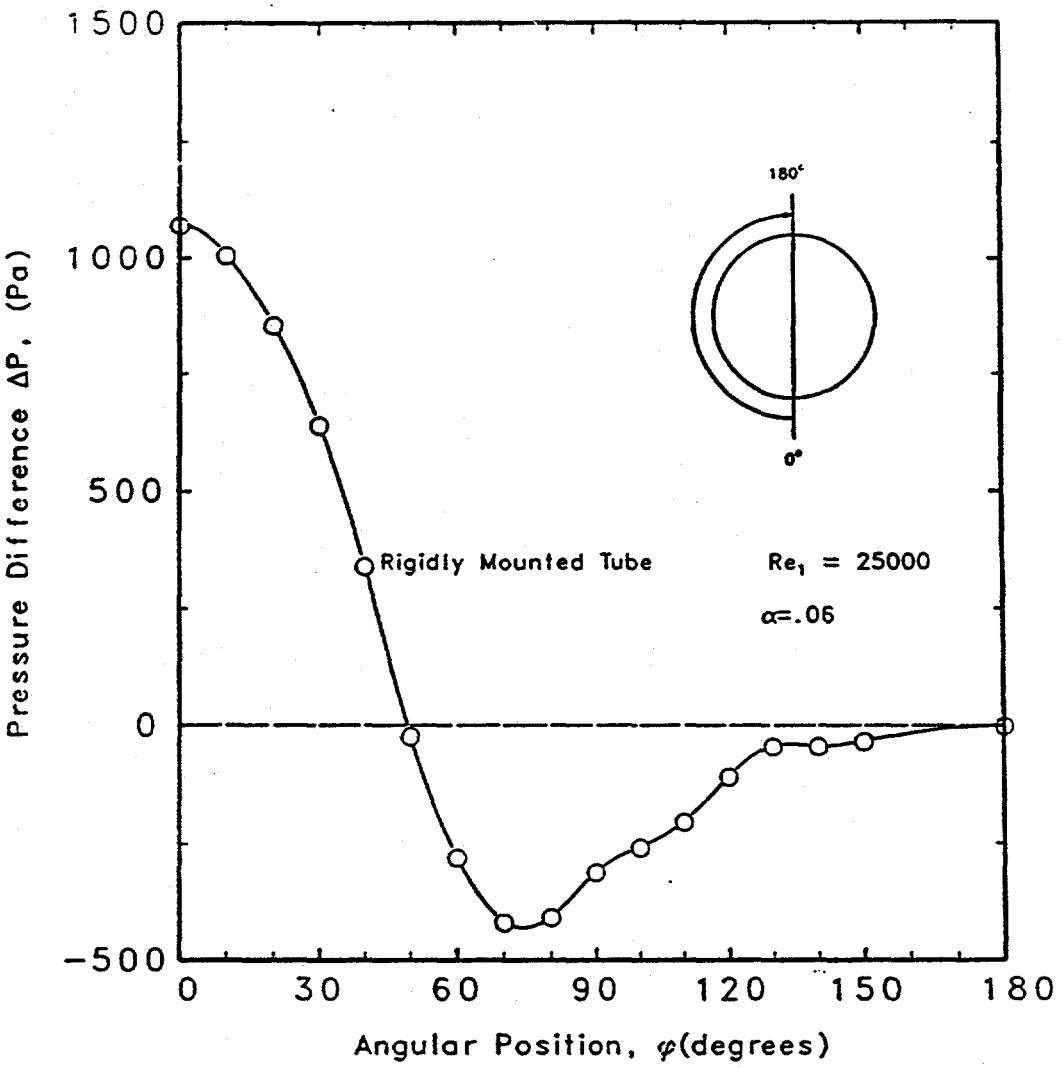

Figure 14 – Pressure Distribution About Tube
From Yokosawa et al.

manner, for comparison. The data shown here are for a Reynolds number range of 2.5×10^4 to 1.3×10^5, and a void fraction of 0.06. In the paper, they plotted the pressure coefficient, defined as:

$$Cp_{sur} = \frac{(p_{sur} - p_\infty)}{\Delta p_0} \tag{4.1}$$

where p_{sur} is the static pressure on the cylinder surface, and p_∞ is what the static pressure which would be at the same position without the test cylinder, while the pressure distribution in Figure 14 is plotted is the difference between that at the position about the tube and that at the upper stagnation point, for comparison with the results given in Figure 13. (1 Pa is equivalent to about 500 mm water on our scale.) This was done by using the following equation:

$$\Delta P = \Delta p_0 (Cp_{sur\phi} - Cp_{sur180}) \tag{4.2}$$

Figure 15 is a vertical void profile, also for a freestream void fraction of 0.25, and at a Reynolds number of 1304. Approaching the tube from below, the void fraction is seen to gradually increase until just below the lower stagnation point, while a decrease in void fraction (a "bubble wake") is detected immediately downstream of the cylinder, which gradually returns to the freestream value. This is further illustrated in Figure 16, a plot of the circumferential void profile at various radii, for the same conditions of liquid Reynolds number and freestream void fraction. It had been expected that centrifugal force on the liquid would encourage the bubbles to move towards the cylinder, but as the profiles indicate, they are following the

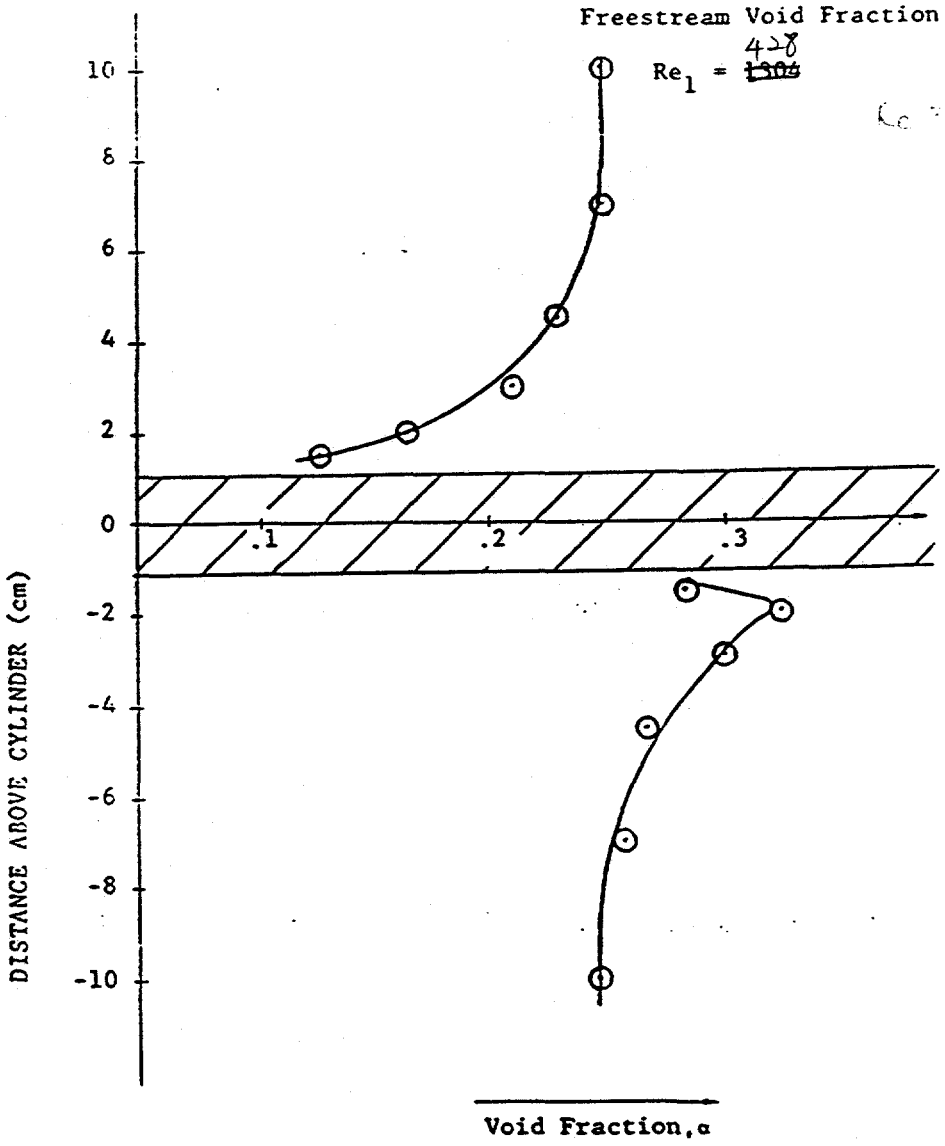

Figure 15. Vertical Void Fraction Profile

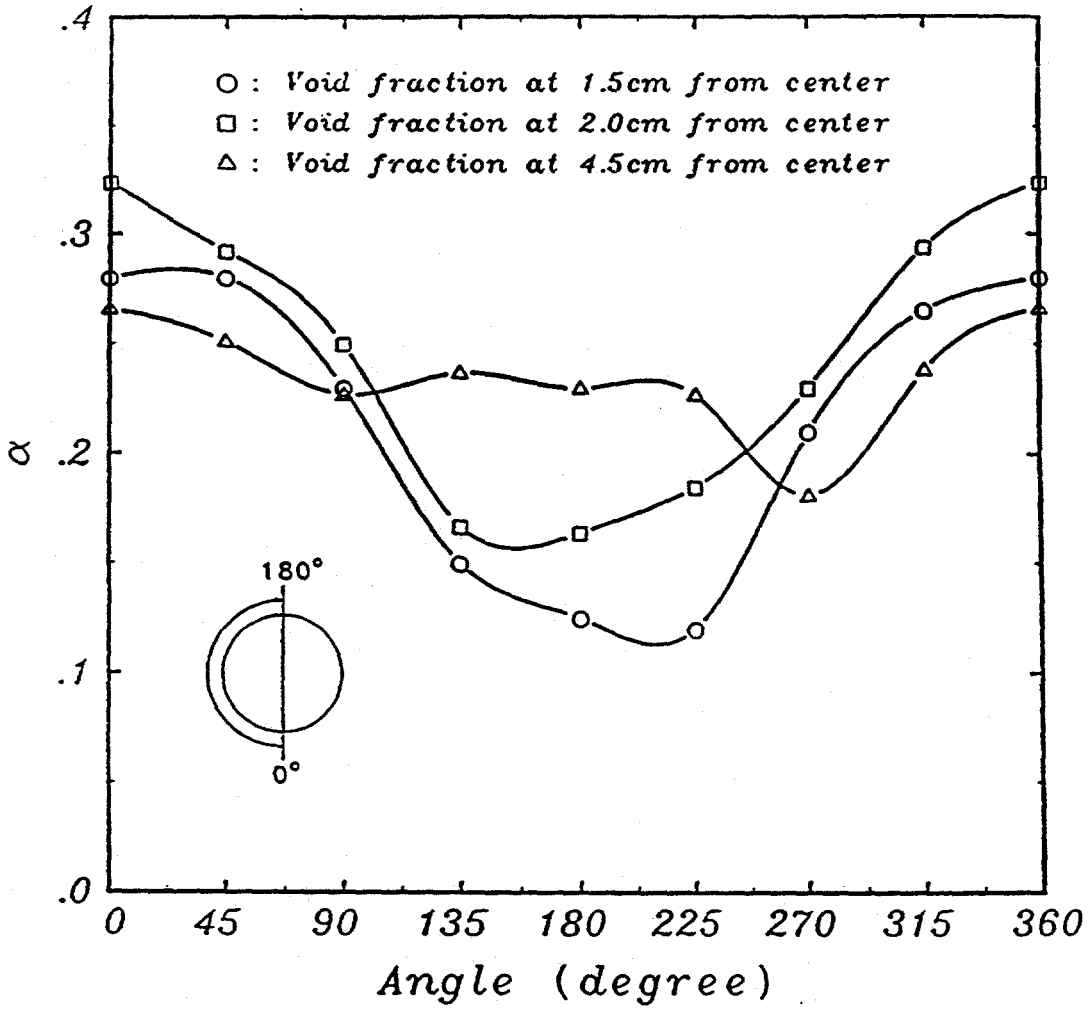

Figure 16. angle vs void fraction

surface of the tube to its equator, and then buoyancy is causing them to rise straight up. Figures 17 and 18, vertical and circumferential void profiles at a liquid Reynolds number of 8226 and a freestream void fraction of 0.25, indicate that the buoyancy effect is somewhat diminished at higher flow rates. The wake in bubbles illustrated by the circumferential void profiles is compatible with the pressure distribution data, as is the slight horizontal asymmetry in void profile which might cause a weak lift force. However, the lift coefficients measured were weak, with random sign changes, and are considered to be error, as mentioned earlier.

Figure 19 shows the drag coefficient for a rigidly mounted cylinder in a normal triangular array of tubes, plotted versus void fraction, for Reynolds numbers of 4703, 17429, and 32683. Plotted on the same figure is the correlation found by Żukauskas (1989), for single phase flow. When the values in this figure for a Reynolds number of 17429 are compared to those in Figure 11 for a Reynolds number of 15427,at the same void fractions, it can be seen that the drag coefficient on a cylinder in an array of tubes has comparable to that on a single cylinder, when the Reynolds number based on the gap velocity is the same as that of the single tube.

The pressure distribution for a Reynolds number of 17429 and a void fraction of 0.25, found by the pressure taps, is plotted in Figure 20, going around the tube starting at the lower stagnation point. The plotted pressure difference is the difference in pressure from that at the upper stagnation point. The freestream velocity of the flow is the same as that of the flow in Figure 13, and a comparison of the two

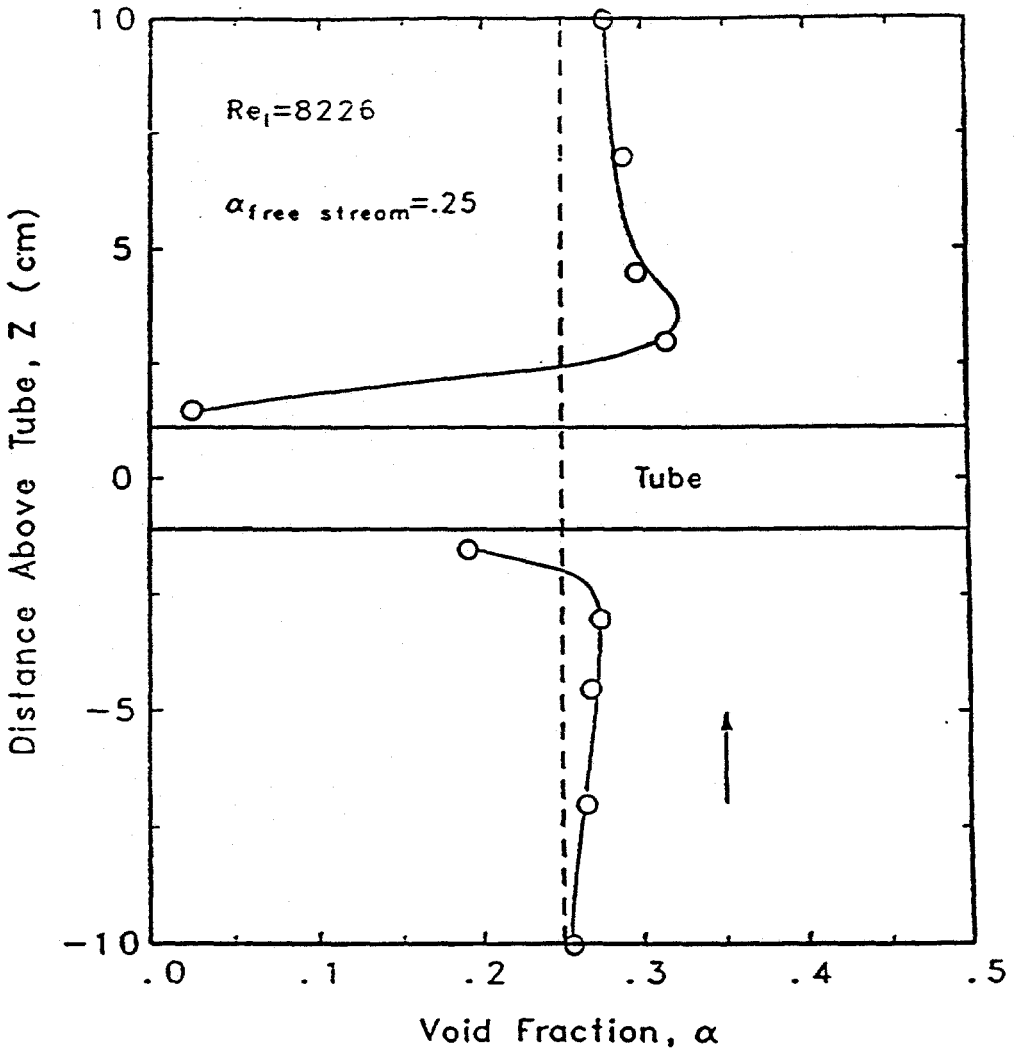

Figure 17. Vertical Void Fraction Profile

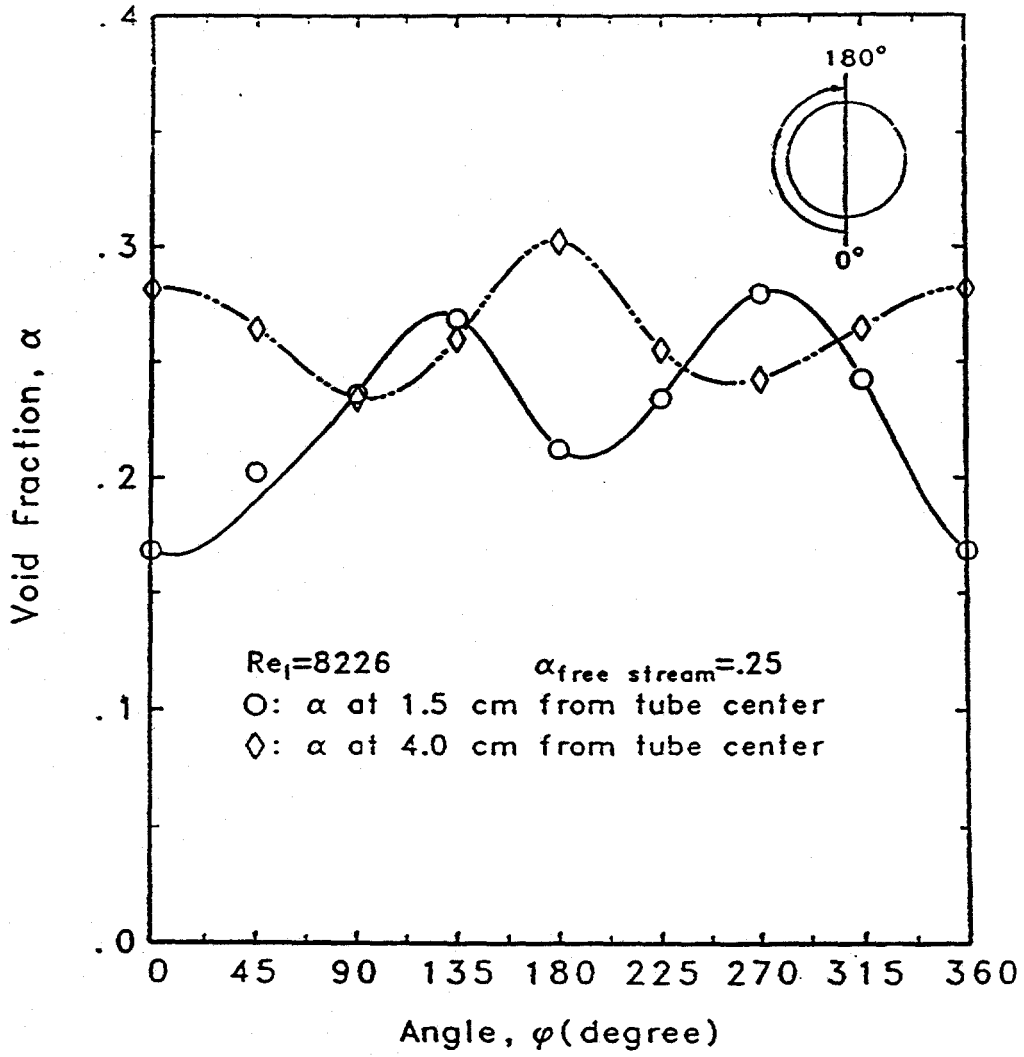

Figure 18. Radial Void Fraction Profile

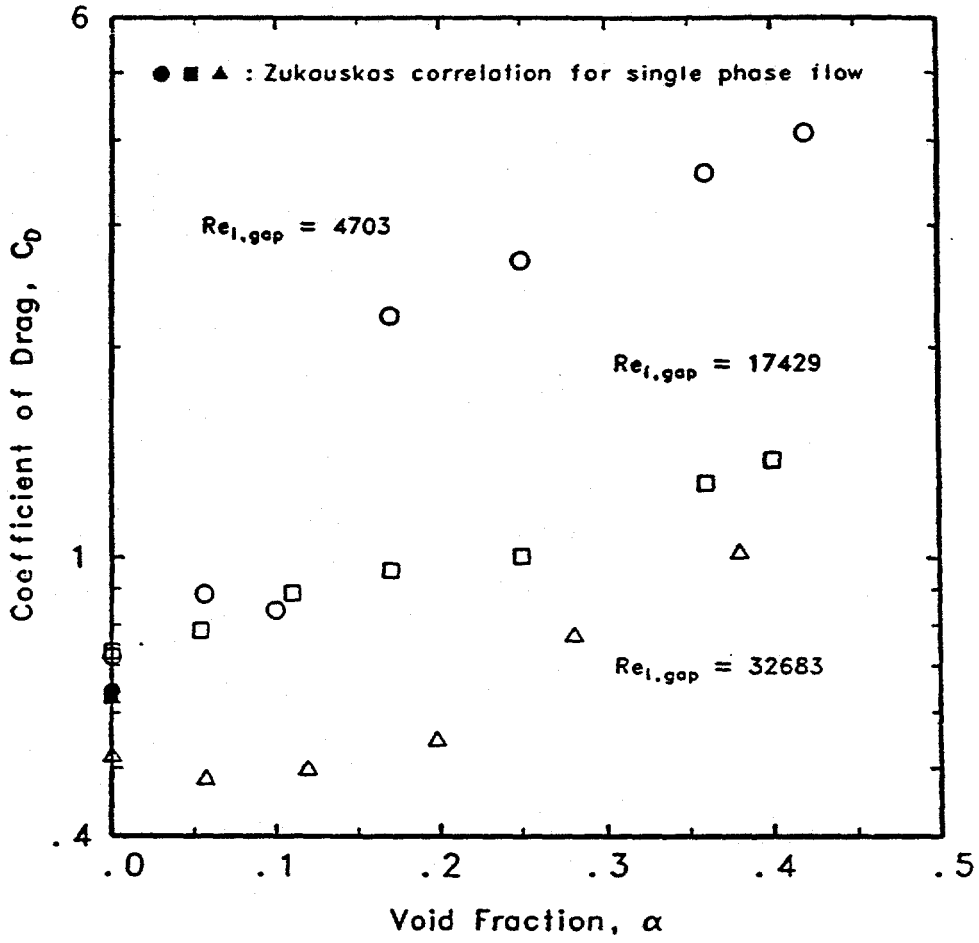

Figure 19 – Coefficient of Drag Over a Rigid Tube in an Array

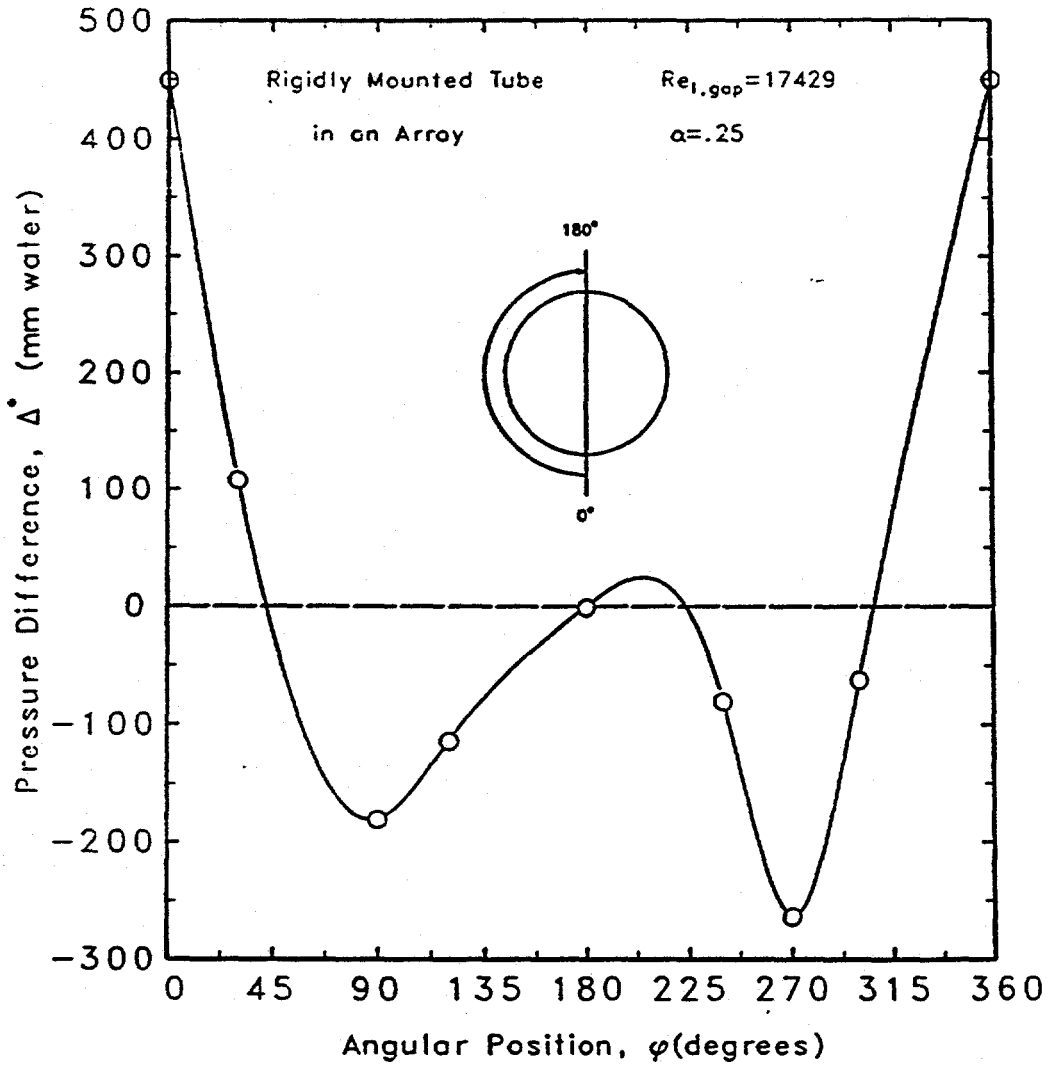

Figure 20 – Pressure Distribution About Tube

plots shows that the magnitude of the pressures is increased with the additional tubes, but the shape of the curve is qualitatively similar.

V Discussion of Results for a Flexibly Mounted Tube

For a flexibly mounted tube, observations were made of drag coefficient, lift coefficient, and pressure distribution. The data are tabulated in Tables 2E to 2G of Appendix 2. The coefficients of drag on a single flexibly mounted tube are plotted versus void fraction, for various Reynolds numbers, in Figure 21. The results are not noticably different from those for a rigidly mounted tube. Again, increasing void fraction is found to very strongly increase the drag coefficient at lower Reynolds numbers, and to more weakly increase the drag coefficient at higher Reynolds numbers.

In Figure 22, the drag coefficient data are again plotted, this time versus Reynolds number for various void fractions, including $\alpha = 0$. Again, the well established correlation found by Roshko (from Sabersky, Acosta, and Hauptmann [1971]) is included. The Reynolds numbers tested at zero void fraction still come within 15% of the correlated values.

The pressure distribution for a Reynolds number of 8226 and a void fraction of 0.25, obtained from the pressure taps, is plotted in Figure 23, with angular position starting from the lower stagnation point. The pressure plotted is again the difference in pressure from that at the upper stagnation point. The mean lift coefficient still is not quite zero, and is tabulated in Appendix 2. When the lift coefficients for a flexibly mounted tube at a Reynolds number of 8226 are compared to those for a rigidly mounted tube at the same Reynolds number (see tables 2B.1f and 2F.1b),

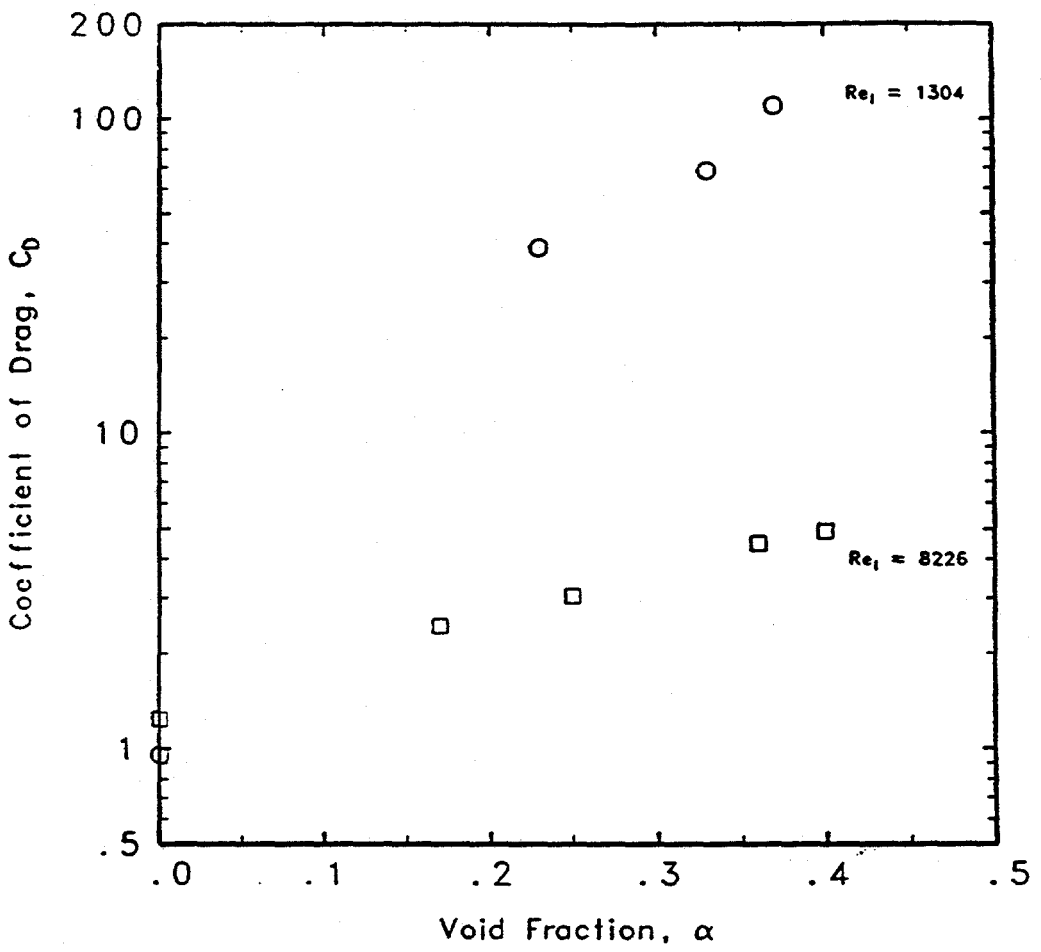

Figure 21 – Coefficient of Drag Over a Single Flexibly Mounted Tube

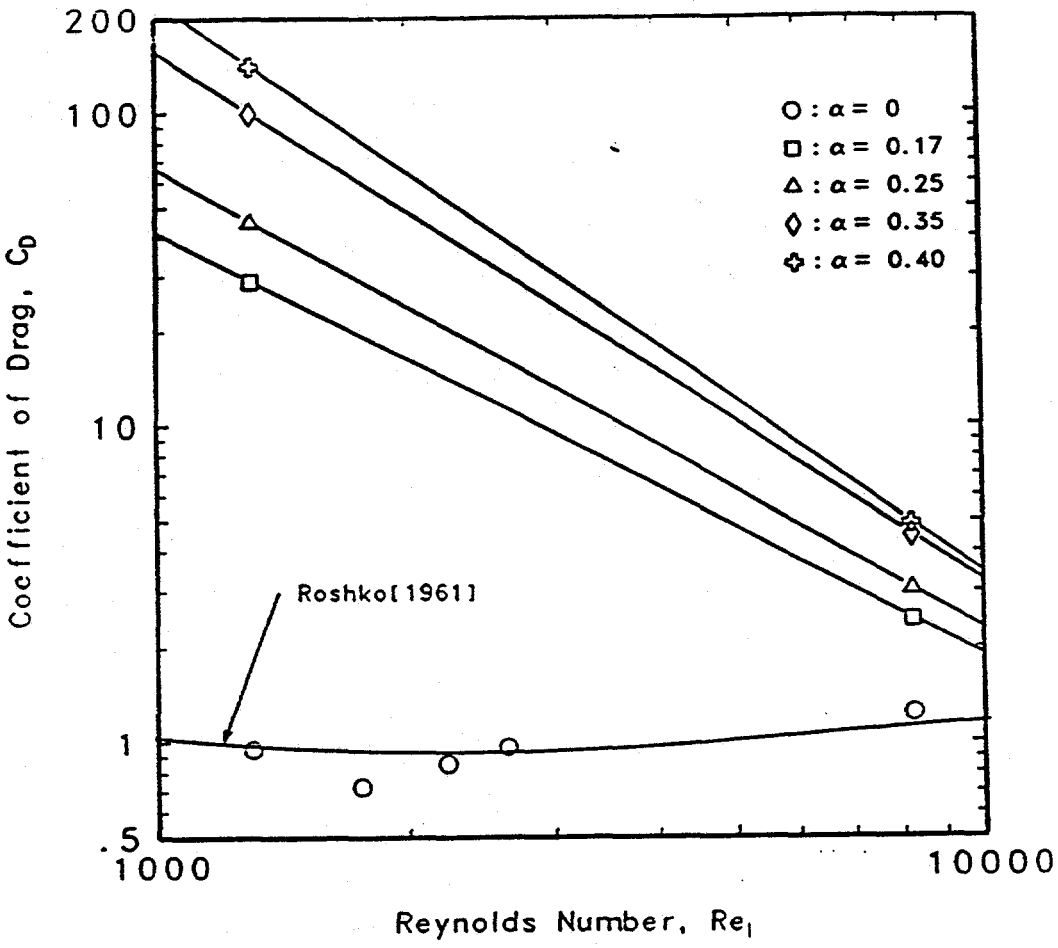

Figure 22 – Coefficient of Drag Over a Single Flexibly Mounted Tube

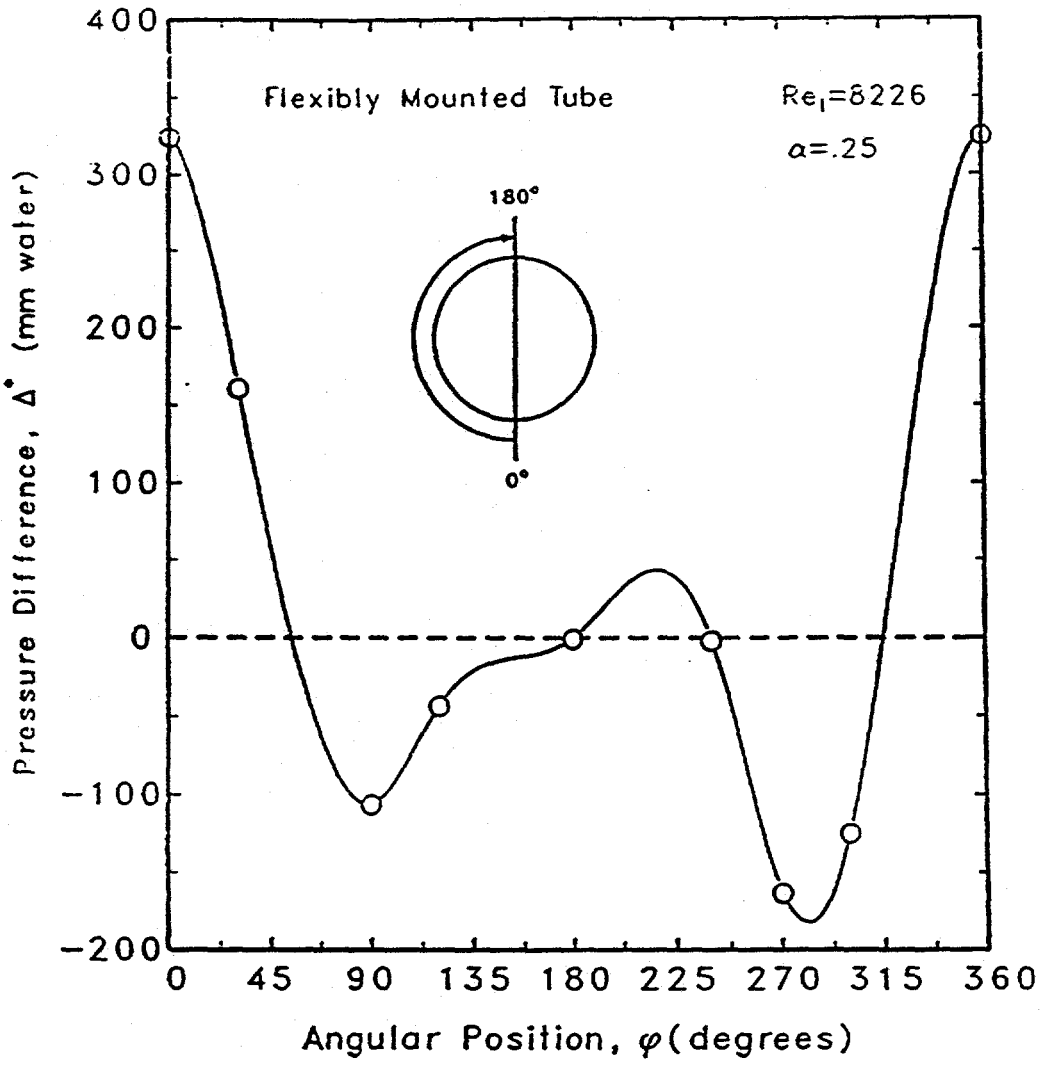

Figure 23 – Pressure Distribution About Tube

it can be seen that the lift coefficient on the flexibly mounted tube tends to be slightly smaller than that on the rigidly mounted tube, although this is not always the case. The randomness seen in the comparison strengthens the argument that the lift exists due to experimental uncertainty.

VI Conclusions

1. The drag coefficient over a single cylinder, whether rigidly or flexibly mounted, is very strongly increased by the addition of air at low Reynolds numbers. As the Reynolds number based on superficial liquid velocity increases, the effect of the addition of air is diminished.

2. At very high Reynolds numbers, the effect on the drag coefficient by the addition of air changes from that experienced at lower Reynolds numbers. By the time the Reynolds number reaches a value of 22000, the addition of a small amount of air in the flow actually decreases the drag coefficient slightly, and as the void fraction increases, the drag coefficient eventually returns to the single-phase value, and then continues to increase.

3. At lower Reynolds numbers, the air bubbles in the flow tend to follow the tube to its equator, and then the buoyancy forces on them overcome any centrifugal forces, and cause them to rise. At higher Reynolds numbers, the centrifugal forces begin to overcome the buoyancy forces, and a higher concentration of bubbles begins to collect behind the tube.

4. There is not much difference between the drag coefficient on a rigidly mounted tube, and that on a flexibly mounted tube. All differences measured were within the uncertainty of the data. There also is not much difference between the drag coefficient on a single tube and that on a tube located within an array.

References

1. Blevins, R.D., Flow-Induced Vibration, 2nd ed. 1990, Van Nostrand Reinhold (New York)

2. Chen, S.S., and Jendrzejczyk, J.A., "Fluid Excitation Forces Acting on a Square Tube Array," Journal of Fluids Engineering, Vol.109, pp 415-423, 1987

3. Connors, H.J., "Fluidelastic Vibration of Tube Arrays Excited by Crossflow," ASME WAM - Symposium on Flow-Induced Vibration in Heat Exchangers, pp 42-56, Dec. 1970

4. Fung, Y.C., "Fluctuating Lift and Drag Acting on a Cylinder in a Flow at Supercritical Reynolds Numbers," Journal of the Aerospace Sciences, Vol.27, No.11, pp 801-813, 1960

5. Goyder, H.G.D., "Fluidelastic Instability and Buffeting of Heat Exchanger Tube Bundles Due to Single and Two-Phase Flows," ASME Symposium, Vol. 2, pp 151-168, 1988

6. Hara, F., "Air Bubble Effects on Vortex-Induced Vibrations of a Circular Cylinder," ASME Symposium on Flow-Induced Vibrations, Vol.1, pp 103-113,Dec. 1984

7. Inoue, A., Kozawa, Y., Yokosawa, M., and Aoki, S., "Studues on Two-Phase Crossflow. Part I: Flow Characteristics Around a Cylinder," International Journal

of Multiphase Flow, Volume 12, No.2, pp 149-167, 1986

8. Mulcahy, T.M., "Fluid Forces on a Rigid Cylinder in Turbulent Cross-Flow," Excitation and Vibration of Bluff Bodies in Cross-Flow, Vol. 1, ASME Winter Annual Meeting, New Orleans, December,1984, pp 15-28

9. Pettigrew, M.J., Tromp, J.H., Taylor, C.E., and Kim, B.S., "Vibration of Tube Bundles in Two-Phase Cross-Flow: Part 2 - Fluidelastic Instability," Proceedings of ASME Int. Symposium on Flow-Induced Vibrations and Noise, WAM, Vol.3, 1988

10. Price, S.J., and Paidoussis, M.P., "The Aerodynamic Forces Acting on Groups of Two and Three Circular Cylinders When Subject to a Crossflow," Journal of Wind Engineering and Industrial Aerodynamics, Vol.17, pp 329-347, 1984

11. Roshko, A., "Experiments on the Flow Past a Circular Cylinder at Very High Reynolds Number," Journal of Fluid Mechanics, Vol. 10, pp 345-356, 1961

12. Sabersky, R.H., Acosta, A.J., and Hauptmann, E.G., Fluid Flow: A First Course in Fluid Mechanics, 2nd ed., 1971, Macmillan Publishing Co., Inc. (New York)

13. Savkar, S.D., "Buffeting of Cylindrical Arrays in Crossflow," Vibrations of Arrays of Cylinders in Cross-Flow, Vol.2, ASME Winter Annual Meeting, New Orleans, December, 1984, pp 195-210

14. Sin, V.K., and So, R.M.C., "Local Force Measurements on Finite-Span

Cylinders in a Cross-flow," Journal of Fluids Engineering, Transactions of the ASME, Vol.109, pp 136-143, 1987

15. Taylor, C.E., Pettigrew, M.J., Axisa, T., and Villard, B., "Experimental Determination of Single and Two-Phase Cross Flow- Induced Forces on Tube Rows," ASME, FIV, PVP Vol.104, pp 31-39, 1986

16. Taylor, C.E., Currie, I.G., Pettigrew, M.J., and Kim, B.S., "Vibration of Tube Bundles in Two-Phase Cross-Flow: Part 3 - Turbulence-Induced Excitation," Proceedings of ASME Int. Symposium on Flow-Induced Vibrations and Noise, WAM, Vol.3, pp 105-129, 1988

17. Yokosawa, M., Kozawa, Y., Inoue, A., and Aoki, S., "Studies on Two-Phase Crossflow. Part II: Transition Reynolds Number and Drag Coefficient," International Journal of Multiphase Flow, Vol.12, No.2, pp 169-184, 1986

18. Yokosawa, M., Kozawa, Y., Inoue, A., and Aoki, S., "Studies on Two-Phase Crossflow. Part III: Characteristics of Unsteady Flow Behavior," International Journal of Multiphase Flow, Vol.12, No.2, pp 185-202, 1986

19. Žukauskas, A., High-Performance Single-Phase Heat Exchangers, revised and augmented ed., 1989, Hemisphere Publishing Corp., pp 241-259

Appendices

Appendix 1 - Error Analysis

The sources of error for these experiments included error in void fraction measurements, error in Reynolds number measurements, and error in the forces measured. Each of these will be discussed below.

Error in Void Fraction:

The void fraction measurements were made using the gamma densitometer and were evaluated with the following equation:

$$\alpha = \frac{ln(I/I_l)}{ln(I_a/I_l)} \tag{3.1}$$

The first source of error in the void fraction measurements which will be discussed is the error due to limitations of the gamma densitometer. This includes inaccuracy in the measurements of I, I_a, and I_l. The resulting error in void fraction, $\frac{\Delta\alpha}{\alpha}$ is found using the formula

$$\Delta\alpha = ((\frac{\delta\alpha}{\delta I}\Delta I)^2 + (\frac{\delta\alpha}{\delta I_l}\Delta I_l)^2 + (\frac{\delta\alpha}{\delta I_a}\Delta I_a)^2)^{1/2} \tag{A1.1.1}$$

Substitute

$$\frac{\delta\alpha}{\delta I} = \frac{1}{Iln(I_a/I_l)} \tag{A1.1.2}$$

$$\frac{\delta\alpha}{\delta I_l} = \frac{\alpha - 1}{I_l ln(I_a/I_l)} \tag{A1.1.3}$$

and

$$\frac{\delta\alpha}{\delta I_a} = \frac{-ln(I/I_l)}{I_a(ln(I_a/I_l))^2} \tag{A1.1.4}$$

to get:

$$\Delta\alpha = \frac{1}{ln(I_a/I_l)}((\Delta I/I)^2 + (\frac{(\alpha-1)\Delta I_l}{I_l})^2 + (\frac{-\alpha\Delta I_a}{I_a})^2)^{1/2} \qquad (A1.1.5)$$

which will henceforth be referred to as $\Delta\alpha_{count}$. $\frac{\Delta\alpha_{count}}{\alpha}$ was usually found to be under ±10%, but for void fractions below 20%, it could be as high as ±21%.

For void profiles taken very near the tube, errors in the void fraction due to errors in the measuring position also arose. If the distance of the beam from the tube center is called r, then the total error in void fraction could be calculated as:

$$\Delta\alpha = ((\Delta\alpha_{count})^2 + (\frac{\delta\alpha}{\delta r}\Delta r)^2)^{1/2} \qquad (A1.1.6)$$

and the total error in void fraction was usually found to be under ±12% of the void fraction, but for void fractions below 20%, it could be as high as ±60% of the void fraction.

Error in Reynolds Number:

Liquid Reynolds number is defined by $Re_l = \frac{U_l D}{\nu}$, and sources of error in Reynolds number include error in liquid flow rate, resulting in an error of U_l, and temperature variations, resulting in an error of ν.

The error in flow rate as measured by the turbine flow meter is rated at ±0.25%. Since the superficial liquid velocity is calculated as

$$U_l = \frac{Q_l}{A_{cross-section}} \qquad (A1.2.1)$$

the error in velocity is also ±0.25%.

For the high Reynolds numbers studied using the 1000 GPM pump, a variation in temperature of $\pm 2°C$ was found. In the temperature range of the experiments, this resulted in a variation in kinematic viscosity of $\pm 4.65\%$. The total error in Reynolds number is calculated as:

$$\Delta Re_l = ((\frac{\delta Re_l}{\delta U_l}\Delta U_l)^2 + (\frac{\delta Re_l}{\delta \nu}\Delta \nu)^2)^{1/2} \qquad (A1.2.2)$$

where

$$\frac{\delta Re_l}{\delta U_l} = \frac{D}{\nu} \qquad (A1.2.3)$$

and

$$\frac{\delta Re_l}{\delta \nu} = \frac{-U_l D}{\nu^2} \qquad (A1.2.4)$$

The resulting error in Reynolds number is calculated as:

$$\Delta Re_l = ((\frac{D}{\nu}\Delta U_l)^2 + (\frac{-U_l D}{\nu^2}\Delta \nu)^2)^{1/2} \qquad (A1.2.5)$$

giving an overall error in Reynolds number of $\pm 4.66\%$.

Error in Forces (or in C_D):

Error occurs in the forces measured on the tube for both methods used in the measurements. For the strain gage measurements, the force is directly proportional to the strain readings, so the error in force is simply the same percentage as the error in strain. There are two sources of error for the strain readings, error in calibration, and uncertainty of the measurements. To determine the total error in the strain readings, these two should be directly added. The error in calibration was found to

be ±4%, and the uncertainty of the measurements was ±16.8%, so the total error in strain gage force measurements was ±20.8%. The drag coefficient is calculated as:

$$C_D = \frac{F_D}{1/2\rho_W U_l^2 A} \qquad (A1.3.1)$$

so

$$\frac{\delta C_D}{\delta F_D} = \frac{2}{\rho_W U_l^2 A} \qquad (A1.3.2)$$

and

$$\frac{\delta C_D}{\delta U_l} = \frac{-4F_D}{\rho_W A U_l^3} \qquad (A1.3.3)$$

giving an error in drag coefficient of:

$$\Delta C_D = ((\frac{2}{\rho_W U_l^2 A}\Delta F_D)^2 + (\frac{-4F_D}{\rho_W A U_l^3}\Delta U_l)^2)^{1/2} \qquad (A1.3.4)$$

which has a value of ±4.6%.

The drag coefficients measured using the pressure distribution methods were calculated as:

$$C_D = \frac{gD}{U_l^2}(\frac{\pi\alpha}{2} + \int_0^{2\pi} C_1 \frac{\Delta^*}{D} cos\phi d\phi) \qquad (3.4)$$

This method has possibilities for error in velocity, void fraction, pressure, and angle. Using:

$$\frac{\delta C_D}{\delta U_l} = \frac{-2C_D}{U_l} \qquad (A1.4.1)$$

$$\frac{\delta C_D}{\delta \alpha} = \frac{gD\pi}{2U_l^2} \qquad (A1.4.2)$$

and

$$\frac{\delta C_D}{\delta \phi} = \frac{g\not{D}C_1}{U_l^2\not{D}}\Delta^* cos\phi \qquad (A1.4.4)$$

we obtain:

$$\Delta C_D = ((-\frac{2C_D}{U_l}\Delta U_l)^2 + (\frac{gD\pi}{2U_l^2}\Delta\alpha)^2 + (\frac{gDC_1}{U_l^2 D}\Delta^* cos\phi\Delta\phi)^2)^{1/2} \qquad (A1.4.5)$$

which gives an error in C_D of $\pm 15\%$.

Appendix 2 - Tabulation of Data

This appendix includes tables of data listing the drag coefficients and lift coefficients over both rigidly and flexibly mounted single tubes and tubes in arrays. It also includes data for the pressure distributions about these tubes, in mm of water, as well as data for the void fraction profiles for single rigidly mounted tubes.

Table 2A - Coefficient of Drag Over a Rigid Tube

Table 2A.1 - Single Rigid Tube

Table 2A.1a $Re_l = 371$

Run	α	C_D
(1)	0.16	305.7
(1)	0.23	495
(2)	0.23	429.6
(1)	0.31	720.5
(2)	0.31	773.5
(1)	0.39	1027.1

Table 2A.1b $Re_l = 428$

Run	α	C_D
(1)	0.16	453
(1)	0.23	597.3
(1)	0.31	671.4
(1)	0.39	744.4

Table 2A.1c $Re_l = 1129$

Run	α	C_D
(1)	0.17	48.2
(1)	0.25	77.6
(1)	0.35	111.8
(1)	0.41	124.4
(2)	0.41	116.5
(3)	0.41	120.8

Table 2A.1d $Re_l = 1304$

Run	α	C_D
(1)	0.17	40.75
(1)	0.25	71.3
(1)	0.35	105.6
(1)	0.41	130.7

Table 2A.1e $Re_l = 1922$

Run	α	C_D
(1)	0.17	19.8
(1)	0.25	26.2
(1)	0.35	36.5
(1)	0.41	42.7
(2)	0.41	46.5

Table 2A.1f $Re_l = 2220$

Run	α	C_D
(1)	0.17	18.1
(1)	0.25	24.5
(1)	0.35	38.3
(1)	0.41	46.2

Table 2A.1g $Re_l = 7123$

Run	α	C_D
(1)	0	1.17
(2)	0	1.29
(1)	0.17	2.77
(1)	0.25	3.92
(1)	0.36	6.49
(1)	0.40	7.76

Table 2A.1h $Re_l = 8226$

Run	α	C_D
(1)	0	1.34
(2)	0	1.71
(1)	0.05	2.16
(1)	0.11	2.27
(1)	0.17	2.66
(1)	0.25	2.99
(1)	0.36	4.33
(2)	0.36	4.03
(1)	0.40	4.51
(2)	0.40	4.82

Table 2A.1i $Re_l = 15427$

Run	α	C_D
(1)	0	0.822
(1)	0.052	1.029
(1)	0.110	1.332
(1)	0.182	1.519
(1)	0.263	2.066
(1)	0.360	2.391
(1)	0.413	3.423

Table 2A.1j

$Re_l = 21615, Re_l = 21854$

Re_l	α	C_D
21615	0	1.27
21854	0.046	0.807
21854	0.158	1.377
21854	0.243	1.991

Table 2A.2 - Rigid Tube in an Array

Table 2A.2a $Re_l = 4703$

Run	α	C_D
(1)	0	0.724
(1)	0.056	0.889
(1)	0.10	0.843
(1)	0.17	2.235
(1)	0.25	2.686
(1)	0.36	3.61
(1)	0.42	4.12

Table 2A.2b $Re_l = 17429$

Run	α	C_D
(1)	0	0.736
(1)	0.054	0.788
(1)	0.11	0.892
(1)	0.17	0.962
(1)	0.25	1.01
(1)	0.36	1.29
(1)	0.40	1.39

Table 2A.2c $Re_l = 32683$

Run	α	C_D
(1)	0	0.522
(1)	0.057	0.484
(1)	0.119	0.500
(1)	0.198	0.550
(1)	0.281	0.774
(1)	0.38	1.02

Table 2B - Coefficient of Lift Over a Rigid Tube

Table 2B.1 - Single Rigid Tube

Table 2B.1a $Re_l = 428$

Run	α	C_L
(1)	0.16	-18.8
(1)	0.23	-8.16
(1)	0.31	-21.8
(1)	0.39	+20.4

Table 2B.1b $Re_l = 1304$

Run	α	C_L
(1)	0.17	-2.49
(1)	0.25	-1.54
(1)	0.35	+3.85
(1)	0.41	-5.16

Table 2B.1c $Re_l = 1922$

Run	α	C_L
(1)	0.41	+0.84

Table 2B.1d $Re_l = 2220$

Run	α	C_L
(1)	0.17	+1.21
(1)	0.25	0.74
(1)	0.35	-0.31
(1)	0.41	-0.55

Table 2B.1e $Re_l = 7123$

Run	α	C_L
(1)	0	0.25
(1)	0.17	0.50
(1)	0.25	0.90
(1)	0.36	1.56
(1)	0.40	1.70

Table 2B.1f $Re_l = 8226$

Run	α	C_L
(1)	0	0.0867
(2)	0	0.135
(1)	0.05	0.043
(1)	0.11	-0.0104
(1)	0.17	-0.0163
(1)	0.25	-0.130
(2)	0.25	+0.169
(1)	0.36	-0.379
(2)	0.36	-0.5168
(1)	0.40	-0.825
(2)	0.40	-0.483

Table 2B.1g $Re_l = 15427$

Run	α	C_L
(1)	0	-0.0603
(1)	0.052	-0.102
(1)	0.11	+0.0225
(1)	0.182	+0.0439
(1)	0.263	-0.0018
(1)	0.36	-0.0258
(1)	0.413	-0.0380

Table 2B.1h $Re_l = 21615$

Run	α	C_L
(1)	0	0.1330
(1)	0.046	0.0284
(1)	0.158	0.2168
(1)	0.243	0.0394

Table 2B.2 - Rigid Tube in an Array

Table 2B.2a $Re_l = 4703$

Run	α	C_L
(1)	0	0.024
(1)	0.056	-0.472
(1)	0.10	-0.266
(1)	0.17	-0.414
(1)	0.25	-0.444
(1)	0.36	-0.698
(1)	0.42	-0.635

Table 2B.2b $Re_l = 17429$

Run	α	C_L
(1)	0	-0.0071
(1)	0.054	-0.00091
(1)	0.11	-0.068
(1)	0.17	-0.112
(1)	0.25	-0.054
(1)	0.36	-0.057
(1)	0.40	-0.032

Table 2B.2c $Re_l = 32683$

Run	α	C_L
(1)	0	-0.197
(1)	0.057	-0.115
(1)	0.119	+0.0565
(1)	0.198	-0.330

Table 2C - Pressure Distribution About a Rigid Tube

Table 2C.1 - Single Rigid Tube

Table 2C.1a $Re_l = 428$

ϕ	$\Delta^*(\alpha = 0.16)$	$\Delta^*(\alpha = 0.23)$	$\Delta^*(\alpha = 0.31)$	$\Delta^*(\alpha = 0.39)$
0°	103.5mm	115mm	131.5mm	151.5mm
30°	78mm	84mm	68mm	83.5mm
60°	23.5mm	-41.5mm	-71.5mm	-113.5mm
120°	5mm	-56mm	-83.5mm	-79.5mm
180°	0mm	0mm	0mm	0mm
270°	-13.5mm	-78.5mm	-127mm	-154.5mm
300°	22mm	-28mm	-91mm	-132mm
330°	66.5mm	64mm	56.5mm	76mm
360°	103.5mm	115mm	131.5mm	151.5mm

Table 2C.1b $Re_l = 1304$

ϕ	$\Delta^*(\alpha = 0.17)$	$\Delta^*(\alpha = 0.25)$	$\Delta^*(\alpha = 0.35)$	$\Delta^*(\alpha = 0.41)$
0°	94mm	163mm	228mm	285mm
30°	59mm	108mm	153mm	195mm
60°	-20mm	-10mm	-47mm	-18mm
120°	1mm	-14mm	-39mm	-44mm
180°	0mm	0mm	0mm	0mm
270°	-48mm	-73mm	-117mm	-123mm
300°	-26mm	-34mm	-47mm	-69mm
330°	65mm	117mm	170mm	198mm
360°	94mm	163mm	228mm	285mm

Table 2C.1c $Re_l = 2220$

ϕ	$\Delta^*(\alpha = 0.173)$	$\Delta^*(\alpha = 0.245)$	$\Delta^*(\alpha = 0.349)$	$\Delta^*(\alpha = 0.41)$
0°	118mm	167mm	259mm	310mm
30°	75mm	112mm	184mm	212mm
60°	-62mm	-73mm	-47mm	-47mm
120°	-5mm	-27mm	-18mm	-35mm
180°	0mm	0mm	0mm	0mm
270°	-50mm	-101mm	-101mm	-130mm
300°	-20mm	-60mm	-51mm	-81mm
330°	87mm	116mm	169mm	198mm
360°	118mm	167mm	259mm	310mm

Table 2C.1d $Re_l = 8226$

o	Δ* (α = 0)	Δ* (α = 0.05)	Δ* (α = 0.11)	Δ* (α = 0.17)	Δ* (α = 0.25)	Δ* (α = 0.36)	Δ* (α = 0.40)
0°	141mm	220mm	244mm	255mm	298mm	395mm	428mm
30°	101mm	130mm	95mm	93mm	134mm	212mm	225mm
90°	-26mm	-52mm	-118mm	-180mm	-249mm	-206mm	-219mm
120°	10mm	53mm	-4mm	-109mm	-113mm	-72mm	-96mm
150°	0mm	0mm	0mm	0mm	0mm	0mm	0mm
240°	9mm	64mm	7mm	-65mm	-110mm	-66mm	-91mm
270°	-9mm	-42mm	-138mm	-216mm	-275mm	-276mm	-285mm
300°	-19mm	52mm	-5mm	-124mm	-188mm	-146mm	-156mm
360°	141mm	220mm	244mm	255mm	298mm	395mm	428mm

Table 2C.1e $Re_l = 15427$

o	Δ^* ($\alpha = 0$)	Δ^* ($\alpha = 0.05$)	Δ^* ($\alpha = 0.11$)	Δ^* ($\alpha = 0.18$)	Δ^* ($\alpha = 0.26$)	Δ^* ($\alpha = 0.36$)	Δ^* ($\alpha = 0.41$)
0°	210mm	191mm	212mm	244mm	294mm	396mm	473mm
30°	81mm	125mm	156mm	187mm	229mm	277mm	328mm
90°	-97mm	-123mm	-164mm	-180mm	-183mm	-154mm	-141mm
120°	-26mm	-42mm	-68mm	-92mm	-80mm	-108mm	-114mm
180°	0mm	0mm	0mm	0mm	0mm	0mm	0mm
240°	-49mm	-50mm	-60mm	-56mm	-85mm	-114mm	-105mm
270°	-91mm	-134mm	-167mm	-194mm	-192mm	-177mm	-157mm
300°	-134mm	-143mm	-165mm	-178mm	-174mm	-221mm	-170mm
360°	210mm	191mm	212mm	244mm	294mm	396mm	473mm

Table 2C.1f $Re_l = 21615, \alpha = 0$, and $Re_l = 21854, \alpha \neq 0$

ϕ	$\Delta^*(\alpha = 0)$	$\Delta^*(\alpha = 0.05)$	$\Delta^*(\alpha = 0.16)$	$\Delta^*(\alpha = 0.24)$
0°	431mm	350mm	486mm	609mm
30°	317mm	266mm	388mm	524mm
90°	-116mm	-268mm	-285mm	-274mm
120°	-16mm	-33mm	-93mm	-95mm
180°	0mm	0mm	0mm	0mm
240°	33mm	-81mm	-32mm	-6mm
270°	-107mm	-193mm	-261mm	-283mm
300°	-155mm	-320mm	-328mm	-328mm
360°	431mm	350mm	486mm	609mm

Table 2C.2 - Rigid Tube in an Array

Table 2C.2a $Re_{l_{gap}} = 4703$

θ	Δ^* ($\alpha = 0$)	Δ^* ($\alpha = 0.056$)	Δ^* ($\alpha = 0.10$)	Δ^* ($\alpha = 0.17$)	Δ^* ($\alpha = 0.25$)	Δ^* ($\alpha = 0.36$)	Δ^* ($\alpha = 0.42$)
0°	14.5mm	34.7mm	41.7mm	65.6mm	78.6mm	86.3mm	95mm
30°	4.3mm	20.2mm	19.7mm	31.1mm	25.1mm	-4.8mm	-10mm
90°	-37.5mm	-39.8mm	-44.3mm	-17.4mm	-20.4mm	-55.3mm	-60mm
120°	-20.5mm	-5.3mm	-9.1mm	-0.9mm	0.1mm	-18.8mm	-27mm
180°	0mm	0mm	0mm	0mm	0mm	0mm	0mm
240°	-11.5mm	-7.3mm	-7.3mm	-4.9mm	-2.6mm	-11.5mm	-10mm
270°	-47.5mm	-64.8mm	-60.8mm	-42.4mm	-50.9mm	-106mm	-119mm
300°	-0.3mm	-38.8mm	-62.8mm	-46.2mm	-50.4mm	-58mm	-49mm
360°	14.5mm	34.7mm	41.7mm	65.6mm	78.6mm	86.3mm	95mm

Table 2C.2b $Re_{l,gap}$ = 17429

o	Δ* (α = 0)	Δ* (α = 0.054)	Δ* (α = 0.11)	Δ* (α = 0.17)	Δ* (α = 0.25)	Δ* (α = 0.36)	Δ* (α = 0.40)
0°	287mm	332mm	376mm	407mm	451mm	522mm	578mm
30°	119mm	153mm	142mm	136mm	109mm	133mm	145mm
90°	-117mm	-108mm	-121mm	-120mm	-180mm	-170mm	-158mm
120°	-70mm	-31mm	-42.3mm	-66.9mm	-113mm	-155mm	-159mm
180°	0mm	0mm	0mm	0mm	0mm	0mm	0mm
240°	-62mm	4.3mm	-16.5mm	-47mm	-80mm	-92mm	-101mm
270°	-131mm	-144mm	-197mm	-224mm	-263mm	-250mm	-240mm
300°	-23mm	-45mm	18.5mm	-19.5mm	-61.5mm	-62mm	-59mm
360°	287mm	332mm	376mm	407mm	451mm	522mm	578mm

Table 2D - Void Fraction Profiles for a Single Rigid Tube

Table 2D.1a $Re_l = 428, \alpha_{f_s} = 0.025$

Gamma Beam Normal to Tube

Run	Distance Above Tube (cm)	α
(1)	−27	0.0249
(3)	−21	0.0237
(1)	−12	0.0223
(3)	−11	0.0287
(3)	−5	0.0246
(1)	−4	0.0161
(3)	−2	0.0263
(3)	+6	0.0330
(1)	+9	0.0341

Table 2D.1b $Re_l = 428, \alpha_{fs} = 0.025$

Gamma Beam Parallel to Tube

Run	Distance Above Tube (cm)	α
(2)	−24	0.0093
(4)	−24	0.0344
(2)	−14	0.0240
(4)	−14	0.0206
(2)	−8	0.0144
(4)	−8	0.0259
(4)	−3	0.0267
(2)	+7	0.0036
(4)	+8	0.0205

Table 2D.2a $Re_l = 428, \alpha_{f_s} = 0.15$

Gamma Beam Normal to Tube

Distance Above Tube (cm)	α
−3.8	0.163
2.1	0.179
4.2	0.165
8.2	0.157
14.2	0.155

Table 2D.2b $Re_l = 428$

Gamma Beam Parallel to Tube

Distance Above Tube (cm)	α ($\alpha_{f_s} = .12$)	α ($\alpha_{f_s} = .15$)
−9	0.122	–
−7	–	0.136
+3	–	0.087
+4	0.083	–
+6	–	0.120
+7	0.108	–
+10	–	0.131
+11	0.117	–
+13	0.124	–

Table 2D.3

$Re_l = 428, \alpha_{fs} = 0.13,$

R = 3 cm from tube center

Gamma Beam Parallel to Tube

ϕ	α
0°	0.174
90°	0.167
135°	0.159
180°	0.110
225°	0.139
270°	0.174

Table 2D.4 $Re_l = 428, \alpha_{f_s} = 0.31$

Gamma Beam Parallel to Tube

ϕ	α at R = 2.3 cm	α at R = 2.8 cm	α at R = 3.3 cm
0°	0.416	0.410	0.402
90°	0.334	0.335	0.326
135°	0.276	0.317	0.311
180°	0.267	0.283	0.293
225°	0.304	0.303	0.308
270°	0.295	0.308	0.282

Table 2D.5a $Re_l = 428, \alpha_{f_s} = 0.25$

Gamma Beam Parallel to Tube

ϕ	α at R = 2.5 cm	α at R = 3.0 cm	α at R = 4.0 cm
0°	0.314	0.306	0.288
90°	0.241	0.238	0.210
135°	0.201	0.214	0.218
180°	0.215	0.218	0.232
225°	0.206	0.226	0.221
270°	0.256	0.258	0.249

Table 2D.5b $Re_l = 428, \alpha_{f_s} = 0.25$

Gamma Beam Parallel to Tube

Distance From Tube (cm)	α Above Tube	α Below Tube
1.5	0.126	0.283
2	0.164	0.324
3	0.211	0.301
4.5	0.230	0.266
7	0.249	0.256
10	0.249	0.244

Table 2D.5c $Re_l = 428, \alpha_{f_s} = 0.25$

Gamma Beam Parallel to Tube

ϕ	α at R = 1.5 cm	α at R = 2.0 cm	α at R = 4.5 cm	α at R = 7.0 cm
0°	0.283	0.324	0.266	0.256
45°	0.265	0.294	0.238	0.189
90°	0.211	0.229	0.181	-
135°	0.119	0.185	0.227	0.192
180°	0.126	0.164	0.230	0.249
225°	0.148	0.167	0.237	0.216
270°	0.235	0.248	0.227	-
315°	0.285	0.292	0.251	0.208

Table 2D.6a $Re_l = 2220, \alpha_{fs} = 0.35$

Gamma Beam Parallel to Tube

Distance From Tube (cm)	α Above Tube	α Below Tube
1.5	0.198	0.322
2	0.245	0.397
3	0.320	0.396
4.5	0.334	0.365
7	0.345	0.361
10	0.348	-

Table 2D.6b $Re_l = 2220, \alpha_{fs} = 0.35$

Gamma Beam Parallel to Tube

ϕ	α at R = 1.5 cm	α at R = 2.0 cm	α at R = 3.0 cm	α at R = 4.5 cm	α at R = 6.0 cm
45°	0.306	0.352	0.382	0.328	0.283
90°	0.268	0.296	0.330	0.279	-
135°	0.225	0.275	0.322	0.317	0.265
225°	0.252	0.287	0.333	0.321	0.276
270°	0.298	0.332	0.342	0.282	-
315°	0.336	0.374	0.389	0.337	0.285

Table 2D.7a $Re_l = 8226$, $\alpha_{fs,1} = 0.25$, $\alpha_{fs,2} = 0.40$

Gamma Beam Parallel to Tube

Distance From Tube (cm)	α_1 Above Tube	α_1 Below Tube	α_2 Above Tube	α_2 Below Tube
1.5	0.024	0.191	0.336	0.212
3	0.315	0.274	0.439	0.432
4.5	0.297	0.268	0.418	0.423
7	0.289	0.265	0.408	0.413
10	0.277	0.256	0.416	0.418

Table 2D.7b $Re_l = 8226$, $\alpha_{f_s} = 0.25$

Gamma Beam Parallel to Tube

Joel. P 23 – P 26 Good data

ϕ	α at R = 1.5 cm	α at R = 2.0 cm	α at R = 3.0 cm	α at R = 4.0 cm
0°	~~0.250~~ 0.169	0.200	0.283	0.282
45°	~~0.237~~ 0.203	0.266	0.278	0.265
90°	0.245 0.259	0.269	0.277	0.235
135°	0.155 0.270	0.297	0.282	0.261
180°	~~0.089~~ 0.213	0.293	0.307	0.303
225°	~~0.315~~ 0.235	0.291	0.287	0.256
270°	0.249 0.280	0.243	0.276	0.243
315°	~~0.253~~ 0.243	0.210	0.279	0.265

Agree with notebook Susan II. P.21 : bad data

Table 2D.7c $Re_l = 8226, \alpha_{f_s} = 0.40$

Gamma Beam Parallel to Tube

ϕ	α at R = 1.5 cm	α at R = 2.0 cm	α at R = 3.0 cm	α at R = 4.0 cm
0°	~~0.389~~, 229	0.332	0.443	0.437
45°	~~0.361~~ 0.307	0.409	0.434	0.398
90°	0.342 0.352	0.395	0.412	0.378
135°	0.290 0.401	0.428	0.423	0.412
180°	0.186 0.348	0.417	0.446	0.448
225°	~~0.451~~ 0.382	0.421	0.420	0.397
270°	0.385 0.369	0.345	0.415	0.393
315°	~~0.390~~ 0.304	0.352	0.436	0.402

Table 2D.7d $Re_l = 8226$,

$\alpha_{fs,1} = 0.25$, $\alpha_{fs,2} = 0.40$

Gamma Beam Parallel to Tube

Distance From Tube (cm)	α_1 Above Tube	α_2 Above Tube
1.5	0.180	0.317
1.6	0.219	0.361
1.7	0.270	0.395
1.8	0.262	0.390
1.9	0.247	0.394
2.0	0.270	0.397
2.1	0.254	0.397
2.5	0.305	0.433

Table 2E - Coefficient of Drag Over a Flexibly Mounted Tube

Table 2E.1 Single Phase Flow

Re_l	C_D
1304	1.037
1751	0.730
2220	0.863
2628	0.973

Table 2E.2 $Re_l = 1304$

Run	α	C_D
(1)	0	0.88
(2)	0	1.04
(1)	0.23	39.26
(1)	0.33	69.11
(1)	0.37	110.8

Table 2E.3 $Re_l = 8226$

α	C_D Strain	C_D Press.
	Gages	Dist.
0	1.31	1.22
0.17	1.87	2.74
0.25	2.38	3.20
0.36	3.16	4.82
0.40	3.48	5.05

Table 2F - Coefficient of Lift Over a Flexibly Mounted Tube

$Re_l = 8226$

Run	α	C_L
(1)	0	0.019
(2)	0	-0.0571
(1)	0.17	0.131
(2)	0.17	0.0778
(1)	0.25	-0.127
(2)	0.25	-0.163
(1)	0.36	0.086
(2)	0.36	-0.0996
(1)	0.40	0.291
(2)	0.40	-0.0186

Table 2G - Pressure Distribution About a Flexibly Mounted Tube

$Re_l = 8226$

ϕ	Δ^* ($\alpha = 0$)	Δ^* ($\alpha = 0.17$)	Δ^* ($\alpha = 0.25$)	Δ^* ($\alpha = 0.36$)	Δ^* ($\alpha = 0.40$)
0°	95mm	270.5mm	325.5mm	491.5mm	575.8mm
30°	51mm	143.5mm	161.5mm	256mm	276.8mm
90°	-11mm	-25.3mm	-105.7mm	-95.5mm	-100.1mm
120°	-30mm	-7.5mm	-43mm	-31mm	-8.4mm
180°	0mm	0mm	0mm	0mm	0mm
240°	-1mm	22.8	-1.25mm	48mm	103.8
270°	-40mm	-37mm	-162.5mm	-171.6mm	-189.8mm
300°	15mm	71mm	-124mm	-101.5mm	-75.5mm
360°	95mm	270.5mm	325.5mm	491.5mm	575.8mm

Appendix 3 - Derivation of Equations for Coefficient of Drag and Coefficient of Lift

Equation 3.3:

If P_1 is the pressure at the angle ϕ about the cylinder, and P_2 is the pressure at $\phi + 180°$, then the total upwards force on the cylinder per unit length is:

$$F_t = 2\int_0^{\pi/2} \frac{D}{2}(P_1 - P_2)cos\phi d\phi \qquad (A3.1.1)$$

and

$$P_1 - P_2 = \rho_W g(\delta + C_1\Delta) \qquad (A3.1.2)$$

where C_1 depends upon the angle of the manometers, Δ is the pressure difference read on the manometers, in mm, and δ is the vertical distance between the cylinder surface at ϕ and at $\phi + \pi$, or

$$\delta = Dcos\phi \qquad (A3.1.3)$$

for a cylinder of diameter D. The total force is now:

$$F_t = D\int_0^{\pi/2} (D\rho_W g cos^2\phi + \rho_W g C_1 cos\phi)d\phi \qquad (A3.1.4)$$

or

$$F_t = \frac{\pi}{4}D^2\rho_W g + D^2\int_0^{\pi/2} \rho_W g C_1 \frac{\Delta}{D} cos\phi d\phi \qquad (A3.1.5)$$

The buoyancy force is:

$$F_b = \rho_W g \frac{\pi D^2}{4}(1 - \alpha) \qquad (A3.1.6)$$

so the drag , which is $F_D = F_t - F_b$ is:

$$F_D = \frac{\pi}{4}D^2\rho_W g\alpha + D^2\int_0^{\pi/2} \rho_W g C_1 \frac{\Delta}{D} cos\phi d\phi \qquad (A3.1.7)$$

since

$$C_D = \frac{F_D}{\frac{1}{2}\rho_W U^2 D}$$

we have:

$$C_D = \frac{2gD}{U^2}(\frac{\pi}{4}\alpha + \int_0^{\pi/2} C_1 \frac{\Delta}{D} cos\phi d\phi) \tag{3.3}$$

Equation 3.4:

If P_0 is the pressure at the upper stagnation point of the cylinder, and P is the pressure at the angle ϕ about the cylinder from the lower stagnation point, then:

$$\frac{P_0 - P}{\rho_W g} = \delta + C_1\Delta^* \tag{A3.2.1}$$

where C_1 depends upon the angle of the manometers, Δ^* is the pressure difference between ϕ and the upper stagnation point read on the manometers, in mm, and δ is the vertical distance between the cylinder surface at ϕ and at the lower stagnation point, or

$$\delta = \frac{D}{2}cos\phi - \frac{D}{2} \tag{A3.2.2}$$

for a cylinder of diameter D.

If the total force per unit length on the cylinder is called F_t, and is positive in the upstream direction, then:

$$\frac{F_t}{\rho_W g} = \int_{\phi=0}^{\phi=2\pi} D/2 \frac{P_0 - P}{\rho_W g} cos\phi d\phi \tag{A3.2.3}$$

or

$$\frac{F_t}{\rho_W g} = \int_0^{2\pi} \frac{D}{2}(\delta + C_1\Delta^*)cos\phi d\phi \tag{A3.2.4}$$

$$\int_0^{2\pi} \frac{D}{2}\delta cos\phi d\phi = \int_0^{2\pi} \frac{D^2}{4}(cos\phi - 1)cos\phi d\phi \qquad (A3.2.5)$$

$$= \frac{D^2}{4}\int_0^{2\pi}(cos^2\phi - cos\phi)d\phi = \frac{\pi D^2}{4} \qquad (A3.2.6)$$

so:

$$\frac{F_t}{\rho_W g} = \frac{\pi D^2}{4} + \int_0^{2\pi} C_1\Delta^* \frac{D}{2} cos\phi d\phi \qquad (A3.2.7)$$

If F_b is the buoyancy force,

$$\frac{F_b}{\rho_W g} = \frac{\pi D^2}{4}(1-\alpha) \qquad (A3.2.8)$$

and the drag force $F_D = F_t - F_b (A3.2.9)$, so

$$\frac{F_D}{\rho_W g} = \frac{\pi D^2}{4}\alpha + \int_0^{2\pi} C_1\Delta^* \frac{D}{2} cos\phi d\phi \qquad (A3.2.10)$$

By definition of C_D, we have:

$$F_D = \frac{1}{2}\rho U^2 C_D D \qquad (A3.2.11)$$

so

$$\frac{U^2}{2g} C_D D = \frac{\pi D^2}{4}\alpha + \int_0^{2\pi} C_1\Delta^* \frac{D}{2} cos\phi d\phi \qquad (A3.2.12)$$

and finally:

$$C_D = \frac{gD}{U^2}(\frac{\pi}{2}\alpha + \int_0^{2\pi} C_1 \frac{\Delta^*}{D} cos\phi d\phi) \qquad (3.4)$$

Equation 3.5: The lift force on the cylinder is the total force in the horizontal direction, which is:

$$\frac{F_L}{\rho_W g} = -\int_0^{2\pi} D/2 \frac{P_0 - P}{\rho_W g} sin\phi d\phi \qquad (A3.3.1)$$

In the horizontal direction, the contribution by δ becomes zero, so from equation A3.2.1:

$$\frac{F_L}{\rho_W g} = -\int_0^{2\pi} \frac{D}{2} C_1 \Delta sin\phi d\phi \qquad (A3.3.2)$$

By definition of C_L,

$$F_L = \frac{1}{2}\rho_W U^2 C_D D \qquad (A3.3.3)$$

so

$$C_L = -\frac{gD}{U^2}\int_0^{2\pi} C_1 \Delta sin\phi d\phi \qquad (3.5)$$